SIAM J. SCI. COMPUT.
Vol. 34, No. 5, pp. B606–B641


# HIGH-ORDER CURVILINEAR FINITE ELEMENT METHODS FOR LAGRANGIAN HYDRODYNAMICS*

VESELIN A. DOBREV†, TZANIO V. KOLEV†, AND ROBERT N. RIEBEN‡

**Abstract.** The numerical approximation of the Euler equations of gas dynamics in a moving Lagrangian frame is at the heart of many multiphysics simulation algorithms. In this paper, we present a general framework for high-order Lagrangian discretization of these compressible shock hydrodynamics equations using curvilinear finite elements. This method is an extension of the approach outlined in [Dobrev et al., *Internat. J. Numer. Methods Fluids*, 65 (2010), pp. 1295–1310] and can be formulated for any finite dimensional approximation of the kinematic and thermodynamic fields, including generic finite elements on two- and three-dimensional meshes with triangular, quadrilateral, tetrahedral, or hexahedral zones. We discretize the kinematic variables of position and velocity using a continuous high-order basis function expansion of arbitrary polynomial degree which is obtained via a corresponding high-order parametric mapping from a standard reference element. This enables the use of curvilinear zone geometry, higher-order approximations for fields within a zone, and a pointwise definition of mass conservation which we refer to as strong mass conservation. We discretize the internal energy using a piecewise discontinuous high-order basis function expansion which is also of arbitrary polynomial degree. This facilitates multimaterial hydrodynamics by treating material properties, such as equations of state and constitutive models, as piecewise discontinuous functions which vary within a zone. To satisfy the Rankine–Hugoniot jump conditions at a shock boundary and generate the appropriate entropy, we introduce a general tensor artificial viscosity which takes advantage of the high-order kinematic and thermodynamic information available in each zone. Finally, we apply a generic high-order time discretization process to the semidiscrete equations to develop the fully discrete numerical algorithm. Our method can be viewed as the high-order generalization of the so-called staggered-grid hydrodynamics (SGH) approach and we show that under specific low-order assumptions, we exactly recover the classical SGH method. We present numerical results from an extensive series of verification tests that demonstrate several important practical advantages of using high-order finite elements in this context.

**Key words.** hydrodynamics, compressible flow, hyperbolic partial differential equations, Lagrangian methods, finite elements, variational methods, high-order methods, curvilinear meshes

**AMS subject classifications.** 65M60, 76N15, 76L05

**DOI.** 10.1137/120864672

## 1. Introduction.

We are interested in solving the Euler equations of compressible hydrodynamics for the purposes of modeling complex, multimaterial, high-speed flow and shock wave propagation over general unstructured two-dimensional (2D) and three-dimensional (3D) computational domains. Numerical methods for solving such equations can be classified according to two classical points of view: the Eulerian and the Lagrangian descriptions. In the Eulerian case, numerical methods are defined on a fixed, typically Cartesian, computational mesh through which the fluid moves. In contrast, Lagrangian methods are characterized by a computational mesh that moves with the fluid velocity. The advantages, disadvantages, and applications of each ap-

*Submitted to the journal's Computational Methods in Science and Engineering section February 3, 2012; accepted for publication (in revised form) July 17, 2012; published electronically September 20, 2012. This work was performed under the auspices of the U.S. Department of Energy by Lawrence Livermore National Laboratory under contract DE-AC52-07NA27344, LLNL-JRNL-516394.
http://www.siam.org/journals/sisc/34-5/86467.html
†Center for Applied Scientific Computing, Lawrence Livermore National Laboratory, Livermore, CA 94551 (dobrev1@llnl.gov, tzanio@llnl.gov).
‡Weapons and Complex Integration, B-Division, Lawrence Livermore National Laboratory, Livermore, CA 94551 (rieben1@llnl.gov).

proach are well documented (see, for example, [5] and references therein). In this paper, we are concerned exclusively with Lagrangian methods.

Historically, there have been two major approaches for solving the Euler equations in a Lagrangian frame. The first, known as staggered grid hydrodynamics (SGH), employs a spatial discretization where the *thermodynamic* variables density, pressure, and internal energy are approximated as piecewise constant values defined at zone (element) centers and *kinematic* variables such as velocity and accelerations are defined at the mesh nodes (vertices); see [50, 47]. Artificial viscosity, as originally proposed by [49], is used to generate entropy across shock boundaries while still satisfying the Rankine–Hugoniot jump conditions at an appropriate distance away from the shock (typically a few zones). The second major approach, known as cell-centered hydrodynamics (CCH), treats all hydrodynamic variables as zone (or cell) averaged quantities and uses approximate Riemann solvers (in the spirit of Godunov methods) to determine velocities at mesh vertices; see [21, 38, 37]. This process naturally introduces a sufficient level of dissipation at shock boundaries. We note that work has been done which attempts to bridge the conceptual gap between these approaches and identifies many similarities between them [17, 39].

In both SGH and CCH, the node-based kinematic variables are required to be continuous in order to have a well-defined field with which to move the mesh at each discrete time-step, whereas the thermodynamic variables are discontinuous. This is usually referred to as a "single fluid, multiple material" approximation of the general hydrodynamics equations. The distinction of continuous versus discontinuous thermodynamic variables is trivial for the case of constant zone averaged values but becomes important when we consider the more general case of higher-order bases for thermodynamic fields. There is physical motivation for treating these variables in a discontinuous manner since the equation of state of a material is a local property and discontinuous at material interfaces (contact discontinuities). The exact preservation of material interfaces is one of the attractive features of the Lagrangian framework.

Typically, the staggered grid and cell-centered methods employ finite difference or finite volume techniques to compute spatial gradients which are required for calculating forces. For example, in the case of SGH, the forces acting on a given mesh node due to the gradient of the scalar pressure field are computed using the pressure values and mesh coordinates of the zones which share that node. Since the mesh is an evolving quantity throughout the duration of a Lagrangian computation, its quality changes from time-step to time-step and therefore influences the solution accuracy via the strong dependence on local mesh spacing and quality of finite difference/finite volume gradient computations. This strong dependence on local mesh quality leads to the so-called mesh imprinting phenomenon, where a Lagrangian calculation can prematurely terminate due to mesh tangling or an overly restrictive Courant limited time-step. Such mesh-based errors feeds back into the computation in a nonlinear fashion and can therefore be amplified over time leading to nonphysical results such as symmetry breaking and spurious grid vorticity [24]. In addition to mesh imprinting, SGH Lagrangian calculations have long suffered from the so-called hourglass mode instabilities which are caused by the inability of a numerical method to resolve the gradient of the highest frequency spatial mode of a given computational grid (the so-called checkerboard pressure mode). If left unchecked, such modes can grow indefinitely in a time-dependent problem leading to spurious grid distortion. To address this instability, it is often necessary to introduce artificial forces in the momentum equation which are designed to resist (or filter out) the offending modes [25, 48].

The arbitrary Lagrangian–Eulerian (ALE) technique was developed largely to overcome many of these issues [30, 4, 31, 20]. In a typical ALE implementation, the mesh is evolved in a Lagrangian manner until the element quality deteriorates, at which point it is adjusted according to some prescribed quality metrics. This remeshing step is followed by the remap phase, where the solution variables are conservatively and monotonically remapped onto the new mesh. The ALE technique is a very mature methodology and is the basis for many large-scale, massively parallel simulation codes. Though we do not consider the details of ALE in this paper, we point out that the Lagrange step, where the equations are discretized on a computational mesh which has been moved with the fluid, is at the core of every ALE method. It is also important to emphasize that despite its many advantages in maintaining mesh quality and general robustness, ALE will not solve the underlying errors in symmetry and energy conservation that are generated by the Lagrange step.

There has been much work in developing improvements to both the SGH and the CCH approach. The so-called compatible hydro approach of [10, 13, 3] was developed to overcome several of the long-standing deficiencies of Lagrangian methods, including the inability of many numerical methods to exactly conserve the total energy. The compatible method introduces the notions of subzonal *corner masses* and corresponding *corner forces*, which are used to compute work terms for updating the internal energy in a manner which conserves total energy exactly. Furthermore, the corner masses are used to infer subzonal pressure changes which are then used to compute internal zone forces designed to resist hourglass mode deformations, and zone "collapse" and, in general, to improve the robustness of Lagrangian computations. Taking a different approach to improving the quality of Lagrangian methods, several researchers have advocated the use of improved artificial viscosities for SGH formulations such as the edge and tensor artificial viscosity formulations of [15, 12, 11, 32]. Similar work has been done for the case of CCH Lagrangian methods by improving the way in which nodal velocities are obtained, as in [39].

Recently, there has been interest in the application of the finite element method (FEM) [18] to the Euler equations and in exploring the connections between FEM and the traditional SGH approaches. In [44, 45] the authors introduce the use of stabilized $Q_1$, $P_1$, and $Q_1/P_0$ elements for multiscale Lagrangian hydrodynamics where they make use of many techniques from finite element theory, such as parametric element mappings, mass and stiffness matrices, and mass lumping, to formulate their methods. Furthermore, a connection between the compatible hydro method and traditional FEMs is described in [1]. While these low-order finite element schemes have shown some promise, there has been relatively little research in high-order approaches for Lagrangian computations. Notable exceptions are [34], where a discontinuous Galerkin-type method with an acoustic Riemann solver on triangular grids is described; [7], which introduces a high-order cell-centered scheme where the edges of each zone are parametrized by rational quadratic Bezier curves; and [16], where a third-order ENO-based scheme on topologically structured 2D meshes with quadratically curved edges is proposed.

The goal of this paper is to present another contribution to this research area, which centers on a generalized FEM treatment of the compressible hydrodynamics equations, that includes the case of higher-order basis functions obtained via a high-order mapping from a reference element. To focus the presentation, we restrict ourselves to 2D and 3D Cartesian geometry, but our finite element discretization framework has a very natural extension to 2D axisymmetric problems, which we discuss in [23]. Our method is built around the notion of general high-order

polynomial basis function representations for the various Lagrangian state variables. This leads to many novel features, including curvilinear zone geometries (also explored in [40, 16]), the notion of strong mass conservation which is a pointwise generalization of zonal mass conservation, high-order continuous velocities (e.g., biquadratic, bicubic, biquartic), high-order discontinuous thermodynamic variables, the generalization of the "corner force" concept to high-order cases which leads to total discrete energy conservation by construction, a high-order treatment of the tensor artificial viscosity, novel variants of the artificial viscosity coefficient to account for curvilinear zone geometry, and the generalization of the subzonal pressure method of [14] by treating the equations of state as functions which vary inside of a zone. Furthermore, we show that our general method exactly reduces to classical SGH under specific low-order assumptions. As pointed out in [16], curvilinear meshes are essential for higher-order accuracy. This is another motivation for our approach, which extends to *arbitrary order* elements on unstructured 2D and 3D grids.

The remainder of this paper is organized as follows. In section 2 we review the derivation of the continuum equations of Lagrangian hydrodynamics and introduce some notation. In section 3 we consider an abstract finite dimensional variational formulation of the Euler equations in a Lagrangian frame. The description and the results in this section are fairly general and remain valid for a large variety of kinematic and thermodynamic discretization spaces. In section 4 we present a specific finite element numerical algorithm based on the general semidiscrete Lagrangian framework which uses high-order finite element spaces defined on curvilinear zone geometries obtained through a high-order mapping from a reference element. In section 5 we prove equivalence of the resulting general finite element formulas to some classical SGH methods under simplifying, low-order approximations. In section 6 we discuss the details of the artificial viscosity terms we use in the general high-order methods and introduce several novel concepts for treating the artificial viscosity coefficient in this context. In section 7 we apply a generic time discretization process to the semidiscrete equations and develop the fully discrete computational algorithm. Finally, in section 8 we present an extensive series of numerical results from several verification tests solved using the newly develop method and demonstrate its practical advantages over a wide scope of problem types.

**2. Conservation laws of Lagrangian hydrodynamics.** Consider a continuous medium, $\Omega(t)$, e.g., a fluid or elastic body which is deforming in time. We think of the medium as composed of a continuum number of particles, $\{x(t)\}$, which occupy different points in space for different values of $t$. The initial configuration at time $t = t_0$ will be denoted by $\widetilde{\Omega} \equiv \Omega(t_0)$ and its particles by $\{\tilde{x}\}$. In the Lagrangian description of motion, the particle position $x$ is expressed as a function of the initial position $\tilde{x}$ and time:

$$x = x(\tilde{x}, t) = \widetilde{\Phi}(\tilde{x}, t)\,, \quad \tilde{x} \in \widetilde{\Omega}\,, \quad t \geq t_0\,. \tag{2.1}$$

This description corresponds to an observer moving with the medium and is characterized by the use of the material derivative

$$\frac{d\alpha}{dt}(x,t) = \frac{d}{dt}[\alpha(x(\tilde{x},t),t)] \quad \text{or} \quad \frac{d\alpha}{dt} = \frac{\partial \alpha}{\partial t} + v \cdot \nabla \alpha\,. \tag{2.2}$$

Here $\alpha = \alpha(x,t)$ is any quantity (scalar, vector, etc.) associated with the fluid, while $v$ is the particle velocity, i.e., the rate of change of the particle position relative to an outside observer (or Eulerian reference frame):

$$v(x,t) = \frac{dx}{dt} \equiv \frac{\partial \widetilde{\Phi}(\tilde{x},t)}{\partial t}\,. \tag{2.3}$$

Note that in (2.2) and the rest of the paper we use the derivative and contraction operators according to general tensor rules; e.g., $(v\cdot\nabla v)_j = \sum_i v_i(\partial_i v_j)$.

The conservation laws of Lagrangian hydrodynamics are a direct consequence of the following result, known as the *Reynolds transport theorem* (see, e.g., [43, 36]), which describes the rate of change of integrated quantities (mass, momentum, energy, etc.):

$$\frac{d}{dt}\int_{U(t)} \alpha = \int_{U(t)} \frac{d\alpha}{dt} + \alpha\,\nabla\cdot v\,. \tag{2.4}$$

Here $U(t) = \widetilde{\Phi}(\widetilde{U},t)$ is an arbitrary control volume (a set of particles), which deforms in time starting from an original configuration $\widetilde{U} \subseteq \widetilde{\Omega}$.

The Reynolds transport theorem can be derived using a change of variables and the identity

$$\frac{d|\widetilde{J}|}{dt} = |\widetilde{J}|\,\nabla\cdot v\,, \tag{2.5}$$

where $\widetilde{J} = \nabla_{\tilde{x}}\, x = \nabla_{\tilde{x}}\widetilde{\Phi}$ is the Jacobian of the Lagrangian transformation (2.1) and $|\widetilde{J}|$ is its determinant.

Setting $\alpha = 1$ in (2.4) gives the so-called geometric conservation law (GCL)

$$\frac{d|U(t)|}{dt} = \int_{U(t)} \nabla\cdot v\,, \tag{2.6}$$

where $|U(t)|$ denotes the volume of $U(t)$.

**2.1. Mass conservation.** Let $\rho$ be the density (mass per volume) of the fluid. A fundamental postulate of Lagrangian hydrodynamics is that the mass in any volume $U(t)$ does not change in time:

$$\frac{d}{dt}\int_{U(t)} \rho = 0\,. \tag{2.7}$$

Using the Reynolds transport theorem (2.4), this becomes

$$\int_{U(t)} \frac{d\rho}{dt} = -\int_{U(t)} \rho\,\nabla\cdot v\,, \quad \text{or} \quad \frac{1}{\rho}\frac{d\rho}{dt} = -\nabla\cdot v\,. \tag{2.8}$$

Equivalently, using a change of variables $U(t) \to \widetilde{U}$ via (2.1), the mass conservation law (2.7) can also be expressed as

$$\frac{d}{dt}(\rho|\widetilde{J}|) = 0 \quad \text{or} \quad \rho(x,t)|\widetilde{J}(\tilde{x},t)| = \rho(\tilde{x},t_0)\,, \tag{2.9}$$

where $x = \widetilde{\Phi}(\tilde{x},t)$ and $\tilde{x} \in \widetilde{\Omega}$, $t$ are arbitrary. When used directly for discretization, we refer to the above identity as the *strong mass conservation* principle to emphasize that it is equivalent with exact mass conservation for any Lagrangian volume.

Note that the Reynolds transport theorem (2.4) and (2.8) imply

$$\frac{d}{dt}\int_{U(t)} \rho\alpha = \int_{U(t)} \rho\frac{d\alpha}{dt}\,, \tag{2.10}$$

which can also be derived directly.

**2.2. Momentum conservation.** Let $\sigma$ be the deformation stress tensor. In the absence of external body forces, the conservation of momentum reads

$$\frac{d}{dt}\int_{U(t)} \rho\, v = \int_{\partial U(t)} n\cdot\sigma\,, \tag{2.11}$$

where $\partial U(t)$ denotes the boundary of the control volume $U(t)$ with unit normal $n$. Using (2.10) and the divergence theorem we get

$$\int_{U(t)} \rho\,\frac{dv}{dt} = \int_{U(t)} \nabla\cdot\sigma \qquad \text{or} \qquad \rho\,\frac{dv}{dt} = \nabla\cdot\sigma\,. \tag{2.12}$$

**2.3. Energy conservation.** Let $e$ denote the internal energy per unit mass. Then, the total internal and kinetic energies in $U(t)$ are given by

$$IE(t) = \int_{U(t)} \rho\, e \qquad \text{and} \qquad KE(t) = \frac{1}{2}\int_{U(t)} \rho\,|v|^2\,, \tag{2.13}$$

respectively, and the total energy is $E(t) = KE(t) + IE(t)$. In the absence of a heat flux, the conservation of total energy can be expressed as

$$\frac{d}{dt}\int_{U(t)} \rho\,\left(e + \frac{1}{2}|v|^2\right) = \int_{\partial U(t)} n\cdot\sigma\cdot v\,. \tag{2.14}$$

Simplifying, using (2.10), the pointwise momentum conservation (2.12), along with the fact that $\nabla\cdot(\sigma\cdot v) = (\nabla\cdot\sigma)\cdot v + \sigma : \nabla v$, we get

$$\int_{U(t)} \rho\,\frac{de}{dt} = \int_{U(t)} \sigma : \nabla v\,, \qquad \text{or} \qquad \rho\,\frac{de}{dt} = \sigma : \nabla v\,. \tag{2.15}$$

**2.4. Equation of state.** In gas dynamics, the stress tensor is isotropic and has the form $\sigma = -p\,I$. Here $p$ is the thermodynamic pressure, which can be expressed as a function of the density and the internal energy through a constitutive relation $p = EOS(\rho, e)$. This function, known as the equation of state, is determined by experiments, and though analytical forms are available in simple cases, in practice it is typically given as tabulated data. In the (simplest) case of a polytropic ideal gas with a constant adiabatic index $\gamma > 1$, the equation of state has the form

$$p = (\gamma - 1)\rho\, e\,. \tag{2.16}$$

**2.5. The Euler equations in differential form.** Combining (2.12), (2.8), (2.15) and (2.16) we can write the system of Euler equations of gas dynamics in a Lagrangian reference frame [29]:

$$\text{momentum conservation:} \quad \rho\frac{dv}{dt} = \nabla\cdot\sigma\,, \tag{2.17}$$

$$\text{mass conservation:} \quad \frac{1}{\rho}\frac{d\rho}{dt} = -\nabla\cdot v\,, \tag{2.18}$$

$$\text{energy conservation:} \quad \rho\frac{de}{dt} = \sigma : \nabla v\,, \tag{2.19}$$

$$\text{equation of motion:} \quad \frac{dx}{dt} = v\,, \tag{2.20}$$

$$\text{equation of state:} \quad \sigma = -EOS(\rho,\, e)I\,. \tag{2.21}$$

We use a general stress tensor $\sigma$ in the above formulation in order to accommodate the inclusion of anisotropic tensor artificial viscosity stresses. Specifically, in section 6 we will replace (2.21) with $\sigma = -pI + \sigma_a$, where $\sigma_a$ will generally depend on all other variables.

The boundary conditions for the Euler equations typically have the form $v \cdot n = g$, enforcing symmetry planes for $g = 0$ or providing a velocity drive for $g \neq 0$.

**3. Abstract semidiscrete Lagrangian variational formulation.** In this section we consider a generic finite dimensional weak variational formulation of the Euler equations in a Lagrangian frame. A semidiscrete method for (2.17)–(2.21) is concerned only with the spatial approximation of the continuum equations and begins with a discretization of the particle space. A specific finite element numerical algorithm based on this framework is presented in section 4. We keep the description in this section general in order to allow for alternative discrete space constructions, such as those with nonnodal bases [19].

**3.1. Discrete kinematic and thermodynamic spaces.** Let $d \in \{1, 2, 3\}$ be the space dimension. The semidiscrete Lagrangian discretization is determined by two finite dimensional spaces on the initial domain $\widetilde{\Omega}$:

- a kinematic space $\mathcal{V} \subset [H^1(\widetilde{\Omega})]^d$ with a basis $\{w_i\}_{i=1}^{N_\mathcal{V}}$,
- a thermodynamic space $\mathcal{E} \subset L_2(\widetilde{\Omega})$ with a basis $\{\phi_i\}_{j=1}^{N_\mathcal{E}}$.

We discretize the position $\{x(t)\}$ using the expansion

$$x(\tilde{x}, t) = \sum_i \mathbf{x}_i(t) w_i(\tilde{x}) = \mathbf{x}(t)^{\mathrm{T}} \mathbf{w}(\tilde{x}) \,, \tag{3.1}$$

where $\mathbf{x}(t)$ is an unknown time-dependent vector of size $N_\mathcal{V}$ and $\mathbf{w}$ is a column vector of all the basis functions $\{w_i\}_{i=1}^{N_\mathcal{V}}$. The vector $\mathbf{x}(t)$ represents the motion of the fluid according to

$$\Omega(t) = \{x(\tilde{x}, t) \ : \ \tilde{x} \in \widetilde{\Omega})\} \,. \tag{3.2}$$

Note that we can define Lagrangian (moving) extensions of the kinematic and thermodynamic basis functions on $\Omega(t)$ through the formulas $w_i(x, t) = w_i(\tilde{x})$ and $\phi_j(x, t) = \phi_j(\tilde{x})$, where $x$ is the position of particle $\tilde{x}$ at time $t$. Due to (2.2), these moving bases are constant along particle trajectories and therefore have zero material derivatives

$$\frac{dw_i}{dt} = 0 \qquad \text{and} \qquad \frac{d\phi_j}{dt} = 0 \,. \tag{3.3}$$

The corresponding moving spaces will be denoted by $\mathcal{V}(t)$ and $\mathcal{E}(t)$, respectively.

A mild restriction on the space $\mathcal{V}$, expressing that we can represent exactly the initial geometry, is the requirement that there is a coefficient vector $\mathbf{x}(t_0)$, such that

$$x(\tilde{x}, t_0) = \mathbf{x}(t_0)^{\mathrm{T}} \mathbf{w}(\tilde{x}) = \tilde{x} \qquad \forall \tilde{x} \in \widetilde{\Omega} \,.$$

This vector also provides the initial conditions for the unknown $\mathbf{x}(t)$.

The discrete velocity field corresponding to the motion (3.1) is given by

$$v(\tilde{x}, t) = \sum_i \frac{d\mathbf{x}_i}{dt}(t) w_i(\tilde{x}) = \mathbf{v}(t)^{\mathrm{T}} \mathbf{w}(\tilde{x}) \,, \quad \text{i.e.,} \quad \mathbf{v} = \frac{d\mathbf{x}}{dt},$$

as in (2.3). Note that we can also think of the velocity as a function on $\Omega(t)$ with the expansion $v(x,t) = \sum_i \frac{d\mathbf{x}_i}{dt}(t) w_i(x,t)$ using the same coordinates, but in the moving kinematic basis. We can also introduce the Jacobian of the discrete motion

$$\widetilde{J}(\tilde{x},t) = \nabla_{\tilde{x}}\, x = \sum_i \mathbf{x}_i(t)\, \nabla w_i(\tilde{x})\,.$$

Since both $v$ and $\widetilde{J}$ are defined as in the continuous case (by differentiating (3.1)), we still have (2.5) as well as the GCL (2.6) on a semidiscrete level.

**3.2. Semidiscrete conservation laws.** Given an initial density field $\rho_0(\tilde{x}) = \rho(\tilde{x}, t_0)$, we use the strong mass conservation principle (2.9) to define the density for all time,

$$\rho(\tilde{x},t) = \rho_0(\tilde{x})/|\widetilde{J}(\tilde{x},t)|, \tag{3.4}$$

which as stated previously implies that the mass in every Lagrangian volume is preserved exactly.

We formulate the discrete momentum conservation equation by applying a variational formulation to the continuous equation (2.17). Using a Galerkin approach (at a given time $t$) we multiply (2.17) by a moving basis test function $w_j \in \mathcal{V}(t)$ and integrate over $\Omega(t)$:

$$\int_{\Omega(t)} \rho \frac{dv}{dt} \cdot w_j = \int_{\Omega(t)} (\nabla \cdot \sigma) \cdot w_j\,. \tag{3.5}$$

Performing integration by parts on the right-hand side, we obtain

$$\int_{\Omega(t)} \rho \frac{dv}{dt} \cdot w_j = -\int_{\Omega(t)} \sigma : \nabla w_j + \int_{\partial\Omega(t)} n \cdot \sigma \cdot w_j, \tag{3.6}$$

where $n$ is the outward pointing unit normal vector of the surface $\partial\Omega(t)$. Assuming the boundary integral term vanishes (which is the case, e.g., for boundary conditions $v \cdot n = 0$ and $\sigma = -pI$) and expanding the velocity in the moving basis gives us

$$\sum_i \frac{d\mathbf{v}_i}{dt} \int_{\Omega(t)} \rho\, w_i \cdot w_j = -\int_{\Omega(t)} \sigma : \nabla w_j\,. \tag{3.7}$$

In other words,

$$\mathbf{M}_{\mathcal{V}} \frac{d\mathbf{v}}{dt} = -\int_{\Omega(t)} \sigma : \nabla \mathbf{w}, \tag{3.8}$$

where $\mathbf{M}_{\mathcal{V}}$ is the *kinematic mass matrix* which is defined by the integral

$$\mathbf{M}_{\mathcal{V}} \equiv \int_{\Omega(t)} \rho \mathbf{w}\mathbf{w}^{\mathrm{T}}\,. \tag{3.9}$$

An important feature of our approach is that this mass matrix is independent of time due to (2.10) and (3.3):

$$\frac{d\mathbf{M}_{\mathcal{V}}}{dt} = \frac{d}{dt}\int_{\Omega(t)} \rho \mathbf{w}\mathbf{w}^{\mathrm{T}} = \int_{\Omega(t)} \rho \frac{d}{dt}(\mathbf{w}\mathbf{w}^{\mathrm{T}}) = 0\,. \tag{3.10}$$

The thermodynamic discretization starts with the expansion of the internal energy in the basis $\{\phi_j\}$:

$$e(\tilde{x},t) = \sum_j \mathbf{e}_j(t)\phi_j(\tilde{x}) = \mathbf{e}(t)^{\mathrm{T}}\boldsymbol{\phi}(\tilde{x})\,,$$

where $\mathbf{e}(t)$ is an unknown time-dependent vector of size $N_{\mathcal{E}}$ and $\boldsymbol{\phi}(\tilde{x})$ is a column vector of all the basis functions $\{\phi_j\}_{j=1}^{N_{\mathcal{E}}}$. The internal energy can also be expressed in the moving thermodynamic basis: $e(x,t) = \sum_j \mathbf{e}_j(t)\phi_j(x,t)$.

Consider a weak formulation of the energy conservation equation (2.19) obtained by multiplying it by $\phi_i$ and integrating over the domain $\Omega(t)$:

$$\int_{\Omega(t)} \left(\rho\frac{de}{dt}\right)\phi_i = \int_{\Omega(t)} (\sigma : \nabla v)\,\phi_i. \tag{3.11}$$

Expressing the energy in the moving thermodynamic basis gives

$$\sum_j \frac{d\mathbf{e}_j}{dt}\int_{\Omega(t)} \rho\phi_j\phi_i = \int_{\Omega(t)} (\sigma : \nabla v)\,\phi_i.$$

In other words,

$$\mathbf{M}_{\mathcal{E}}\frac{d\mathbf{e}}{dt} = \int_{\Omega(t)} (\sigma : \nabla v)\,\boldsymbol{\phi}, \tag{3.12}$$

where $\mathbf{M}_{\mathcal{E}}$ is the *thermodynamic mass matrix* which is defined by the integral

$$\mathbf{M}_{\mathcal{E}} \equiv \int_{\Omega(t)} \rho\boldsymbol{\phi}\boldsymbol{\phi}^{\mathrm{T}}\,. \tag{3.13}$$

Analogous to the kinematic case, we can use the fact that the thermodynamic basis functions have zero material derivatives to conclude that $\mathbf{M}_{\mathcal{E}}$ is independent of time.

We now introduce an $N_{\mathcal{V}} \times N_{\mathcal{E}}$ rectangular matrix $\mathbf{F}$, which we call the *force matrix* that connects the kinematic and thermodynamic spaces:

$$\mathbf{F}_{ij} = \int_{\Omega(t)} (\sigma : \nabla w_i)\,\phi_j\,. \tag{3.14}$$

The stress tensor $\sigma$ is defined using the equation of state and the above density and internal energy fields:

$$\sigma(x,t) = -EOS(\rho(x,t), e(x,t))I\,.$$

By simply changing the above evaluation, our approach can handle general stresses, including strength models and artificial viscosity terms; see section 6. Note, however, that our methods do not require the inclusion of artificial stresses designed to resist hourglass modes or other special deformations.

**3.3. The Euler equations in semidiscrete form.** Given the previous definitions, we can summarize the general semidiscrete Lagrangian conservation laws in the following simple form:

$$\text{momentum conservation:} \qquad \mathbf{M}_{\mathcal{V}}\frac{d\mathbf{v}}{dt} = -\mathbf{F}\cdot\mathbf{1}, \tag{3.15}$$

$$\text{energy conservation:} \qquad \mathbf{M}_{\mathcal{E}}\frac{d\mathbf{e}}{dt} = \mathbf{F}^{\mathrm{T}}\cdot\mathbf{v}, \tag{3.16}$$

$$\text{equation of motion:} \qquad \frac{d\mathbf{x}}{dt} = \mathbf{v}. \tag{3.17}$$

The vector $\mathbf{1}$ above is the representation of the constant one in the thermodynamic basis $\{\phi_i\}$ (we assume that $1 \in \mathcal{E}$). Boundary conditions can be implemented by eliminating the corresponding rows and columns in $\mathbf{M}_\mathcal{V}$ (which will in general introduce a difference between its blocks).

THEOREM 3.1. *The general semidiscrete Lagrangian method* (3.15)–(3.17) *has the following conservation properties: exact total momentum conservation (in any direction), exact GCL* (2.6)*, exact mass conservation, and exact total energy conservation.*

*Proof.* The exact GCL and mass conservation were already discussed in the beginning of this section.

Regarding the total energy conservation, note that the formulas for the total internal and kinetic energies (2.13) can be expressed in the semidiscrete settings as

$$IE(t) = \mathbf{1} \cdot \mathbf{M}_\mathcal{E} \cdot \mathbf{e}\,, \qquad KE(t) = \frac{1}{2}\,\mathbf{v} \cdot \mathbf{M}_\mathcal{V} \cdot \mathbf{v}\,.$$

Therefore the rate of change of the total discrete energy is

$$\frac{dE}{dt} = \frac{d}{dt}\left(\frac{1}{2}\,\mathbf{v} \cdot \mathbf{M}_\mathcal{V} \cdot \mathbf{v} + \mathbf{1} \cdot \mathbf{M}_\mathcal{E} \cdot \mathbf{e}\right).$$

Using the fact that both the kinematic and thermodynamic mass matrices are symmetric and independent of time, as well as (3.15) and (3.16), we get

$$\frac{dE}{dt} = \mathbf{v} \cdot \mathbf{M}_\mathcal{V} \cdot \frac{d\mathbf{v}}{dt} + \mathbf{1} \cdot \mathbf{M}_\mathcal{E} \cdot \frac{d\mathbf{e}}{dt} = -\mathbf{v} \cdot \mathbf{F} \cdot \mathbf{1} + \mathbf{1} \cdot \mathbf{F}^{\mathrm{T}} \cdot \mathbf{v} = 0\,,$$

i.e., the total energy remains constant in time.

Finally, let $c = \mathbf{c}^{\mathrm{T}}\mathbf{w} \in \mathcal{V}$ be a vector function which is constant in space and time, and consider the change of the total momentum in the direction of $c$. By (2.10) and (3.15), we have

$$\frac{d}{dt}\left(c \cdot \int_{\Omega(t)} \rho\, v\right) = \mathbf{c} \cdot \mathbf{M}_\mathcal{V} \frac{d\mathbf{v}}{dt} = -\mathbf{c} \cdot \mathbf{F} \cdot \mathbf{1} = \int_{\Omega(t)} \sigma : \nabla c = 0\,.$$

Thus, the total momentum is also being conserved on a semidiscrete level (provided that constant fields are representable in $\mathcal{V}$). ∎

*Remark* 3.1. Not all discretization methods preserve the GCL on a semidiscrete level. For example, many schemes, such as [50, 47, 13, 14], approximate the velocity divergence in the center of a zone $\Omega_z$ through the rate of change of its volume

$$\frac{1}{|\Omega_z(t)|}\,\frac{d|\Omega_z(t)|}{dt} = \nabla \cdot v\,. \tag{3.18}$$

Though (3.18) is equivalent to (2.6) on quadrilateral meshes, this is no longer the case on general 3D grids (see section 5.1) or 2D axisymmetric grids (see [35, 23]).

**4. Finite element Lagrangian discretization.** In this section we describe a finite element numerical algorithm based on the general semidiscrete Lagrangian discretization method from section 3. The main feature of our approach is the use of high-order kinematic and thermodynamic approximation spaces defined on curvilinear meshes. More details about finite elements can be found in [18, 8, 9].

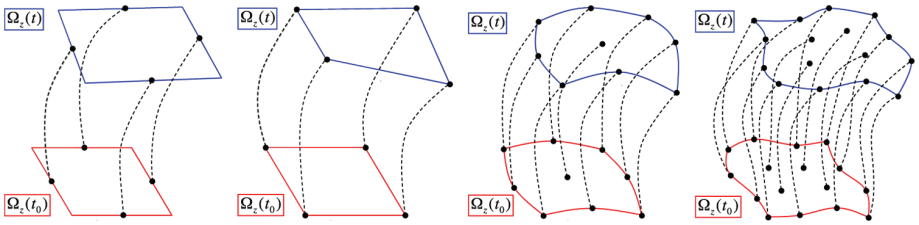


FIG. 4.1. *A zone $\Omega_z(t)$ reconstructed from the evolution of only a few of its points (particles) indicated by black circles. Shown are several choices corresponding to (left to right) Crouzeix–Raviart, $Q_1$, $Q_2$ and $Q_3$ finite elements. Note that the reconstruction with Crouzeix–Raviart elements is not unique and that the zone boundaries are curved in the $Q_2$ and $Q_3$ cases.*

**4.1. Particle motion and geometry reconstruction.** We start with some geometric considerations related to the choice of the finite element kinematic discretization space $\mathcal{V}$ and the definition of the deformed domain $\Omega(t)$.

A natural way to discretize the motion of the whole medium is to describe it through the motion of only a finite number of particles. In practice, we decompose the spatial domain $\Omega(t)$ at the initial time $t = t_0$ into a set of nonoverlapping, discrete volumes $\{\Omega_z(t_0)\}$ called zones (or elements) and associate particles with them; see Figure 4.1. The union of these discrete zones forms the initial computational domain $\widetilde{\Omega}$ which may, in general, be an approximation of the exact initial domain.

After evolving the particles in time, the zones $\Omega_z(t)$ are reconstructed based on the locations of the particles associated with them (vertices, edge midpoints, etc.), thus defining the moved mesh $\Omega(t)$. Note that this reconstruction process introduces a *geometric error* (which should vanish under refinement), since the computational mesh will be only an approximation to the true geometry of the exact domain, even if the particle trajectories are exact.

The presence of this built-in geometric error motivates the use of high-order elements, as the $Q_2$ and $Q_3$ elements shown in Figure 4.1, since such elements have more degrees of freedom on the zone boundaries, allowing them to better represent smooth deformations. High-order elements are also advantageous in representing initial curvature (e.g., at boundaries and interfaces) as well as curvature naturally developing in the flow, as illustrated with the exact solutions of two classical test problems in Figure 4.2.

In section 3 we described a general functional reconstruction approach (3.2) based on abstract particle locations represented by the expansion coefficients $\mathbf{x}(t)$. In the rest of this section we detail a natural way to define a local reconstruction through the FEM [18, 8, 9]. In the settings of section 3 this amounts to defining the basis for the space $\mathcal{V}$ by local construction on each zone. Other reconstruction procedures are also possible; see [40].

**4.2. Finite element curvilinear zone reconstruction.** The finite element space construction begins with definitions on the reference element $\widehat{\Omega}_z$, e.g., the unit square in 2D or the unit cube in 3D. Throughout the remainder of this paper, all quantities which are defined with respect to the reference element coordinate system will be accented with a "hat" symbol.

We consider a basis on the reference element $\{\hat{\eta}(\hat{x})\}_{i=1}^{N_v}$ which is nodal, i.e., there is a set of points called nodes $\{\hat{p}_i\}_{i=1}^{N_v}$ such that $\hat{\eta}_i(\hat{p}_j) = \delta_{ij}$, where $\delta_{ij}$ is the Kronecker delta symbol. The points $\{\hat{p}_i\}$ represent the fixed particle locations on $\widehat{\Omega}_z$ and $\hat{\eta}_i$ is

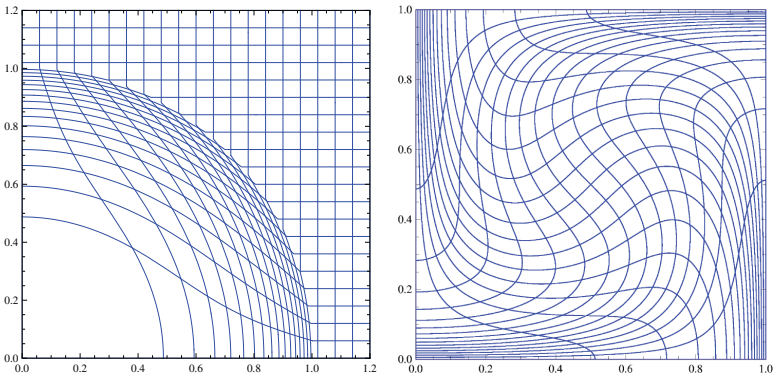

FIG. 4.2. *An initial Cartesian mesh deformed according to the exact solutions of the Sedov blast wave (left) and the Taylor–Green vortex (right). See section* 8.

the (high-order) nodal basis function associated with particle $i$. Given the particle locations $\{x_{z,i}(t)\}$ for a zone $\Omega_z(t)$, we reconstruct the zone by defining the curvilinear zone mapping

$$\Phi_z(\hat{x},t) = \sum_{i=1}^{N_v} x_{z,i}(t)\ \hat{\eta}_i(\hat{x})\,, \tag{4.1}$$

which is defined so that it maps the reference nodes $\{\hat{p}_i\}$ to the particle locations of the zone (see Figure 4.1):

$$\Phi_z(\hat{p}_i,t) = x_{z,i}(t), \qquad i = 1,\dots,N_v\,.$$

Based on this reconstruction, the volume occupied by $\Omega_z(t)$ is the image of the reference zone $\widehat{\Omega}_z$ under the map $\Phi_z$:

$$\Omega_z(t) = \{x = \Phi_z(\hat{x},t) : \hat{x} \in \widehat{\Omega}_z\}\,.$$

For the case of a traditional 2D $Q_1$ zone geometry consisting of four vertices connected by straight lines, the mapping $\Phi_z$ is bilinear. We propose to use high-order mappings such as $Q_2$ (biquadratic) which produce zones with curvilinear geometry.

The global FEM space $\mathcal{V}(t)$ (see section 3) is defined by identifying the particles that share the same physical location, i.e., particles at common zone boundaries. With any global particle $p$ we associate $d$ kinematic vector basis functions of the form

$$w_{i_1} = (\eta_p,0,0), \qquad w_{i_2} = (0,\eta_p,0), \qquad w_{i_3} = (0,0,\eta_p) \qquad \text{in three dimensions.}$$

The scalar function $\eta_p$ is nonzero only in zones $\Omega_z$ that contain the particle $p$. Restricted to $\Omega_z$ it is defined as

$$\eta_p(x,t)|_{\Omega_z} = \hat{\eta}_j(\hat{x}) \qquad \text{with} \quad x = \Phi_z(\hat{x},t)\,, \tag{4.2}$$

where $j$ is the local particle index for $p$ in the zone $\Omega_z$. In this (nodal) FEM setting, the global unknown vector $\mathbf{x}(t)$ consists of the coordinates of all particles. Here, we defined $\mathcal{V}(t)$ directly using the particle trajectories, whereas in section 3 we defined it through $\mathcal{V} = \mathcal{V}(t_0)$. Both approaches are identical. Indeed, the bases agree at $t = t_0$ (by definition) and (4.2) implies that the material derivatives of $w_i$ are zero, which coincides with the definition used in section 3. In particular,

$$\Phi_z(\hat{x},t) = \widetilde{\Phi}(\Phi_z(\hat{x},t_0),t)\,. \tag{4.3}$$

**4.3. Finite element mass conservation.** The element Jacobian matrix is defined as

$$\mathbf{J}_z = \nabla_{\hat{x}} \Phi_z \tag{4.4}$$

and generally varies inside the zone. The determinant of the Jacobian, $|\mathbf{J}_z| \equiv \det \mathbf{J}_z$, gives a measure of volume at a specific point, since the total volume of a Lagrangian zone can be computed as

$$|\Omega_z(t)| = \int_{\widehat{\Omega}_z} \det \mathbf{J}_z(t)\,. \tag{4.5}$$

By differentiating (4.3), we get the following relation between the element Jacobian and the Jacobian of the Lagrangian transformation from section 3:

$$\mathbf{J}_z(t) = \mathbf{J}_z(t_0)\, \widetilde{J}(t)\,. \tag{4.6}$$

A fundamental postulate of the Lagrangian description of hydrodynamics is the fact that the total mass contained within a discrete volume element $\Omega_z$ does not change in time. In other words, if we introduce the "zonal mass"

$$\mathbf{m}_z \equiv \int_{\Omega_z(t)} \rho, \qquad \text{then} \qquad \frac{d\mathbf{m}_z}{dt} = 0\,. \tag{4.7}$$

In both SGH and CCH Lagrangian formulations, the zonal mass is a fundamental quantity and is used to define the evolution of the density as the ratio of the zonal mass to the current volume of the zone. In practice, this is known as "mass conservation by fiat" and it means that the pointwise form of the mass conservation equation in (2.18) is not explicitly discretized.

In contrast, we use our general framework to eliminate the density through the *strong mass conservation principle* (3.4), which in this case takes the form

$$\rho(t) |\det \mathbf{J}_z(t)| = \rho(t_0) |\det \mathbf{J}_z(t_0)|\,. \tag{4.8}$$

Note that the density defined by this equation is not a finite element (or polynomial) function. This is illustrated in Figure 4.3.

The principle of strong mass conservation can be viewed as a generalization of zonal mass conservation as well as the "subzonal mass" concept introduced in [13]. It allows us to define density at any point in time and space as a *function*, which is a critical component of our approach. An alternative approach is to define high-order mass moments, e.g., by projecting the above density in a discontinuous finite element space as in [22].

**4.4. Finite element kinematics.** The momentum conservation equation is discretized following the general framework of section 3 based on the finite element kinematic space from section 4.2.

The locality of the finite element basis implies that the global kinematic mass matrix is sparse and can be computed through a standard finite element assembly procedure from zonal mass matrices:

$$\mathbf{M}_{\mathcal{V}} = \texttt{Assemble}(\mathbf{M}_{\mathcal{V},z})\,.$$

The process of global assembly is analogous to the concept of "nodal accumulation" that is used in a traditional SGH method, where a quantity at a node is defined to be

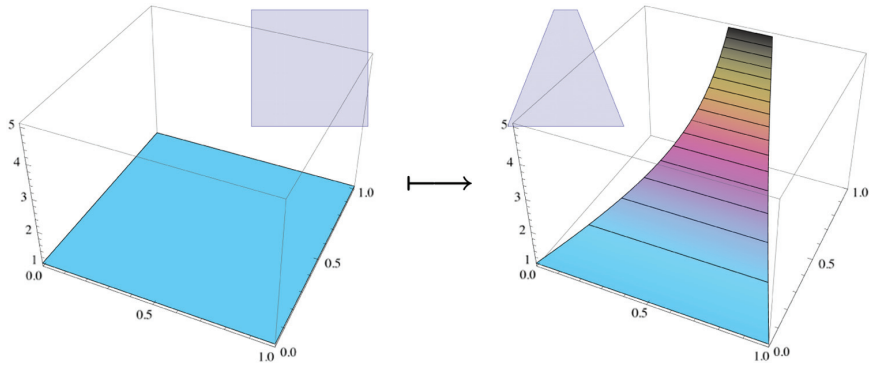


FIG. 4.3. *An initial square zone with* $\rho \equiv 1$ *(left) and the exact density distribution, given by strong mass conservation, after deformation to a trapezoid zone (right).*

the sum of contributions from all of the zones which share this node. For the general high-order case, this means we now have shared degrees of freedom along mesh edges and surfaces in addition to the mesh vertices.

Note that $\mathbf{M}_{\mathcal{V}}$ is symmetric positive definite and block-diagonal (with identical blocks); see (5.2). It is also well-conditioned, which implies that simple conjugate gradient iteration can be used to solve the momentum equation iteratively with optimal efficiency.

Since the kinematic mass matrix is independent of time (see (3.10)), we compute and store $\mathbf{M}_{\mathcal{V}}$ only in the beginning of the simulation. In practice, the local mass matrices $\mathbf{M}_{\mathcal{V},z}$ are computed by transforming the integrals to the reference element and applying a quadrature rule.

**4.5. Finite element thermodynamics.** Since the kinematic degrees of freedom overlap between the zones, it is natural to understand the momentum conservation equation in a global (continuous) sense. In contrast, the equation of state is local, underlining the local character of the density, pressure, and internal energy. Therefore, we argue that the thermodynamic space $\mathcal{E}$ should be discontinuous to allow for restriction of the internal energy conservation equation to the computational zones.

Specifically, to define $\mathcal{E}(t)$ we introduce a thermodynamic basis $\{\hat{\phi}_i\}$ on the reference element and define the global moving basis $\{\phi_j\}$ through the mapping $\Phi_z$. This is done zone-by-zone keeping the zonal degrees of freedom independent, which produces a basis that is discontinuous across zone boundaries. For example, if $j$ is a global degree of freedom corresponding to a local index $i$ in a zone $\Omega_z$, then $\phi_j$ is zero outside of $\Omega_z$ and

$$\phi_j(x,t)|_{\Omega_z} = \hat{\phi}_i(\hat{x}) \quad \text{with} \quad x = \Phi_z(\hat{x},t)\,. \tag{4.9}$$

Following the general framework of section 3 we use $\mathcal{E}(t)$ to discretize the energy conservation equation, locally on each zone. As with the kinematic mass matrix, we can consider the thermodynamic mass matrix as being assembled from the local mass matrices on each individual zone

$$\mathbf{M}_{\mathcal{E}} = \texttt{Assemble}(\mathbf{M}_{\mathcal{E},z})\,.$$

However, due to the discontinuous nature of the thermodynamic basis, there is no sharing of degrees of freedom across zone boundaries and so the "assembled" thermodynamic mass matrix is *block-diagonal* with each block being a purely local matrix on

each zone. Since these local matrices are small and independent of time, we compute and store the inverses $\mathbf{M}_{\mathcal{E},z}^{-1}$ at the beginning of the simulation. In practice, the local mass matrices $\mathbf{M}_{\mathcal{E},z}$ are computed by transforming the integrals to the reference element and applying a quadrature rule.

Note that continuous finite element thermodynamic spaces can also be handled in our framework, though this will introduce interaction between the energies in different zones and will lead to a global matrix $\mathbf{M}_{\mathcal{E}}$.

**4.6. Finite element force matrix.** As with the previously defined mass matrices, the matrix $\mathbf{F}$ from (3.14) can be assembled from zonal contributions:

$$\mathbf{F} = \mathtt{Assemble}(\mathbf{F}_z)\,, \qquad \text{where} \qquad (\mathbf{F}_z)_{ij} \equiv \int_{\Omega_z(t)} (\sigma : \nabla w_i)\, \phi_j.$$

This local rectangular matrix is the high-order generalization of the "corner force" concept described in [13]. It represents the hydrodynamic force contributions from a given zone to a given shared kinematic degree of freedom, as well as the work done by the velocity gradient in the energy equation.

Evaluating $\mathbf{F}_z$ is a locally FLOP-intensive calculation that forms the computational kernel of our finite element discretization method. Specifically, we transform each zone back to the reference element where we apply a quadrature rule with points $\{\hat{q}_k\}$ and weights $\{\alpha_k\}$:

$$(\mathbf{F}_z)_{ij} \approx \sum_k \alpha_k \hat{\sigma}(\hat{q}_k) : \mathbf{J}_z^{-1}(\hat{q}_k) \hat{\nabla} \hat{w}_i(\hat{q}_k)\, \hat{\phi}_j(\hat{q}_k) |\det \mathbf{J}_z(\hat{q}_k)|\,. \tag{4.10}$$

Note that in general, the total stress $\sigma$ is *evaluated at each quadrature point*. In the absence of shear and artificial stresses (see section 6), the total stress is given by $\sigma = -pI$ and the pressure is therefore evaluated at each quadrature point through the equation of state in the evaluation of (4.10). Furthermore, the density (in an equation of state call, for example) is *evaluated at each quadrature point* using the strong mass conservation principle of (4.8). The notion of sampling the density and pressure as functions evaluated at zone quadrature points is a key component of our high-order discretization approach and is essential for robust behavior. Indeed, it is the reason we do not require any special hourglass filters or artificial stresses and is directly analogous to the subzonal pressure method of [14].

*Remark* 4.1. The use of quadrature rules to approximate the integrals in the evaluation of the zonal mass and corner force matrices introduces an additional error in the numerical solution. In practice, we use tensor product Gauss–Legendre quadrature on quadrilateral and hexahedral meshes.

**4.7. Pairs of kinematic and thermodynamic spaces.** Even though the general framework of section 3 allows for arbitrary kinematic and thermodynamic spaces, in practice we have found that $\mathcal{V}$ and $\mathcal{E}$ cannot be chosen independently. This is similar to the classical inf-sup condition for the Stokes problem, but the nonlinear nature of the compressible hydrodynamics equations makes it difficult to formulate and analyze a precise compatibility requirement in our setting. (An inf-sup condition can be derived for the acoustic limit of (2.17)–(2.21) but its usefulness for the nonlinear case is questionable.) The particular choice we focus on in this paper is as follows:

- $\mathcal{V} = (Q_k)^d$, the Cartesian product of the space of continuous finite elements on quadrilateral or hexahedral meshes of order $k$ with reference basis functions of the form $\eta(\hat{x}, \hat{y}) = \sum_{i=1}^{k} \sum_{j=1}^{k} \alpha_{ij} \hat{x}^i \hat{y}^j$;

- $\mathcal{E} = \widehat{Q}_{k-1}$, the companion space of discontinuous finite elements of order one less than the kinematic space.

This choice has been optimal in our numerical experiments, and we refer to it (somewhat informally) as the $Q_k$-$Q_{k-1}$ pair. Analogous construction can be performed on triangular and tetrahedral grids, in which case we denote the pair with $P_k$-$P_{k-1}$.

Another motivation for the above definition is that in the lowest-order case, $k = 1$, we recover the pair $Q_1$-$Q_0$, which, e.g., in two dimensions corresponds to quadrilateral zones with straight edges and piecewise constant thermodynamic variables. This is precisely the choice in many SGH algorithms, and we explore the connection between these schemes and our FEM further in the following section.

**5. Relation to classical discretization schemes.** Below we derive some classical discretization schemes from our general framework under additional discretization assumptions.

**5.1. The staggered grid method of Wilkins.** In this section we show that by using a piecewise bilinear kinematic approximation ($Q_1$) and a single-point quadrature rule with mass lumping, we can exactly recover the traditional staggered-grid method of Wilkins [50] as well as a variant of the method described in [14] on general quadrilateral grids.

The reference zone $\widehat{\Omega}_z$ for quadrilateral grids is the unit square with vertices

$$\hat{X}_1 = (0,0)\,, \quad \hat{X}_2 = (1,0)\,, \quad \hat{X}_3 = (1,1)\,, \quad \hat{X}_4 = (0,1)$$

and corresponding basis functions

$$\hat{\eta}_1(\hat{x},\hat{y}) = (1-\hat{x})(1-\hat{y})\,,\ \hat{\eta}_2(\hat{x},\hat{y}) = \hat{x}(1-\hat{y})\,,\ \hat{\eta}_3(\hat{x},\hat{y}) = \hat{x}\hat{y}\,,\ \hat{\eta}_4(\hat{x},\hat{y}) = (1-\hat{x})\hat{y}\,.$$

The Jacobian matrix for a bilinear mapping to a fixed zone $\Omega_z$ with vertices $\{X_i = (x_i, y_i)\}_{i=1}^4$ has the form

$$\mathbf{J}_z(\hat{x},\hat{y}) = \begin{pmatrix} J_{1,1} & J_{1,2} \\ J_{2,1} & J_{2,2} \end{pmatrix} = \begin{pmatrix} X_2 - X_1 + (X_3 - X_2 - X_4 + X_1)\hat{y} \\ X_4 - X_1 + (X_3 - X_2 - X_4 + X_1)\hat{x} \end{pmatrix}, \tag{5.1}$$

and its inverse can be expressed in terms of its adjugate:

$$\mathbf{J}_z^{-1} = \frac{1}{\det \mathbf{J}_z}\mathbf{J}_Z^{\perp}, \quad \text{where} \quad \mathbf{J}_z^{\perp} = \begin{pmatrix} J_{2,2} & -J_{1,2} \\ -J_{2,1} & J_{1,1} \end{pmatrix}.$$

The zonal kinematic mass matrix is

$$\mathbf{M}_{\mathcal{V},z} = \begin{pmatrix} \mathbf{M}_{\mathcal{V},z}^{xx} & \mathbf{0} \\ \mathbf{0} & \mathbf{M}_{\mathcal{V},z}^{yy} \end{pmatrix}, \ \text{where} \ (\mathbf{M}_{\mathcal{V},z}^{xx})_{ij} = (\mathbf{M}_{\mathcal{V},z}^{yy})_{ij} = \int_{\widehat{\Omega}_z} \rho\hat{\eta}_i\hat{\eta}_j |\det \mathbf{J}_z|\,. \tag{5.2}$$

Note that the determinant of the Jacobian matrix (5.1) is a *linear* function on the reference element. Therefore (4.5) implies that the application of a simple one-point quadrature rule to the mass matrix integral results in

$$\mathbf{M}_{\mathcal{V},z}^{xx} \approx \frac{\rho_z}{16}\,|\Omega_z| O\,,$$

where $O$ is a $4 \times 4$ matrix of ones and $\rho_z$ denotes the value of the density at the zone center. By strong mass conservation (4.8), $\rho_z|\Omega_z|$ is independent of time and equals the zonal mass $m_z$ (4.7).

If we now apply "mass lumping" to $\mathbf{M}_{\mathcal{V},z}^{xx}$ by summing its off-diagonal entries to the diagonal, the global kinematic mass matrix $\mathbf{M}_{\mathcal{V}}$ will be diagonal with entries corresponding to the so-called nodal masses

$$m_n = \sum_{\Omega_z \ni n} \frac{1}{4} \rho_z |\Omega_z| \,.$$

In other words, we can approximate the mass associated with node $n$ by simply adding a quarter of the zone averaged mass of each zone which shares the node. This is precisely the definition of the nodal mass that is used in the method of [50].

To compute the right-hand side of (3.8), we assume $\sigma = -p\, I$ and define the *corner force* vector $\mathbf{f}_z$ at a vertex $j$ (a rearrangement of the $8 \times 1$ matrix $-\mathbf{F}_z$)

$$(\mathbf{f}_z)_j = (\mathbf{f}_z^x, \mathbf{f}_z^y)_j^T = \int_{\Omega_z} p \nabla \eta_j = \int_{\hat{\Omega}_z} p \, (\mathbf{J}_z^{-1} \nabla \hat{\eta}_j) \, |\det \mathbf{J}_z| \,. \tag{5.3}$$

Applying the same one-point quadrature rule to the above integral and substituting the gradients of the bilinear basis functions

$$\nabla \hat{\eta}_1 = (\hat{y} - 1, \hat{x} - 1) \,, \quad \nabla \hat{\eta}_2 = (1 - \hat{y}, -\hat{x}) \,, \quad \nabla \hat{\eta}_3 = (\hat{y}, \hat{x}) \,, \quad \nabla \hat{\eta}_4 = (-\hat{y}, 1 - \hat{x}) \,,$$

as well as the expressions for the term $\mathbf{J}_z^{\perp}$, we arrive at the values

$$\mathbf{f}_z^x = \frac{p_z}{2}(y_2 - y_4, y_3 - y_1, y_4 - y_2, y_1 - y_3) \,, \quad \mathbf{f}_z^y = \frac{p_z}{2}(x_4 - x_2, x_1 - x_3, x_2 - x_4, x_3 - x_1).$$

Here $p_z$ denotes the value of the pressure field $p$ evaluated at the center of the zone. These "corner forces" contribute (by assembling) to the total force representing the right-hand side of the momentum equation for a given node $n$

$$\vec{f}_n = \left( \sum_{\Omega_z \ni n} \mathbf{f}_z^x \,, \sum_{\Omega_z \ni n} \mathbf{f}_z^y \right) ,$$

which is precisely the formula for the so-called HEMP pressure gradient operator of [50]. The HEMP formulas are derived using the control volume on the left in Figure 5.1 by noting that

$$\vec{f}_n = -\frac{1}{2} \sum_k p_k \vec{n}_k \,.$$

We point out that this is also algebraically identical to the compatible hydro method for calculating the pressure gradient as shown in [13]. Indeed, in the notation of Figure 5.1, we have $\vec{n}_1 = \vec{n}_{21} - \vec{n}_{14}$, etc., so by rearrangement of terms

$$\begin{aligned} -2\vec{f}_n &= p_1(\vec{n}_{21} - \vec{n}_{14}) + p_2(\vec{n}_{32} - \vec{n}_{21}) + p_3(\vec{n}_{43} - \vec{n}_{32}) + p_4(\vec{n}_{14} - \vec{n}_{43}) \\ &= (p_4 - p_1)\vec{n}_{14} + (p_3 - p_4)\vec{n}_{43} + (p_2 - p_3)\vec{n}_{32} + (p_1 - p_2)\vec{n}_{21} \,. \end{aligned}$$

The last formula coincides with that in [13] and corresponds to the subzonal control volume on the right in Figure 5.1.

We remark that for constant pressure, the integrand of (5.3) is a bilinear function and therefore a simple one-point quadrature is enough for the *exact* computation of the corner forces. This is not the case in three dimensions, where the integrand is a triquadratic function that requires an eight-point Gaussian rule for exact integration.

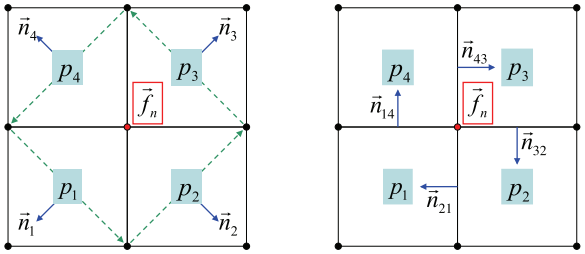


FIG. 5.1. *Schematic depiction of control volume differencing schemes used for computing the node centered gradient of a cell-centered pressure. On the left is the so-called HEMP approach of Wilkins; on the right is the compatible finite difference approach of Caramana et al. Both approaches are algebraically identical for an arbitrary quadrilateral grid and can be derived from a general FEM approach. All normal vectors are of size the length of the edge they are normal to.*

**5.2. The compatible hydro method of Caramana et al.** In [10, 13, 14], the authors introduce the notion of "corner forces," which are used to compute work terms for updating the internal energy of a zone in a manner which conserves total energy algebraically. This is in contrast to so called pdV approach of [50], which computes the change in zone energy by using the change in zone volume.

Here we show that our finite element force matrix corresponds precisely to the corner force approach under the specific approximation choices used in section 5.1 along with the additional choice of a piecewise constant internal energy basis (a single thermodynamic degree of freedom per zone). For each zone, our general high-order semidiscrete energy conservation law reduces to the form

$$\mathbf{M}_{\mathcal{E}} \frac{d\mathbf{e}}{dt} = \mathbf{F}^{\mathrm{T}} \cdot \mathbf{v} \quad \mapsto \quad m_z \frac{de_z}{dt} = -\mathbf{f}_z \cdot \mathbf{v}_z,$$

where $m_z$ is the zonal mass, $e_z$ is the zone averaged value of the internal energy, and $\mathbf{f}_z$ is the collection of corner forces; cf. section 5.1. The total change in energy is therefore given by the inner product $-\mathbf{f}_z \cdot \mathbf{v}_z = -\sum_{n \in \Omega_z} \vec{f}_n \cdot \vec{v}_n$, which is equivalent to the form used in [13].

In [14], subzonal Lagrangian "corner masses" are used to infer subzonal pressure changes, which are then used to compute internal zone forces designed to resist hourglass mode deformations and Lagrangian mesh instabilities. These corner masses are defined in terms of four Lagrangian subvolumes associated with the four vertices of a quadrilateral zone. As in the case of nodal masses for the method of Wilkins, we can derive the subzonal corner masses if we apply a nine-point quadrature rule (obtained by the Cartesian product of the $\left(\frac{1}{4}, \frac{1}{2}, \frac{1}{4}\right)$ composite one-dimensional (1D) trapezoidal rule) followed by mass lumping. Indeed, by linearity the value of the determinant of the Jacobian in the center of a subvolume equals four times its area, and the rest follows analogously to section 5.1 assuming that the density is constant in each subvolume.

**6. Artificial viscosity.** To facilitate the case of shock wave propagation, we now introduce a general tensor artificial viscosity to our semidiscrete equations. The method of artificial viscosity, as originally introduced by Von Neumann and Richtmyer [49], augments the discrete Euler equations with a diffusion term which is scaled by a special mesh dependent, nonlinear coefficient $\mu$. Improvements to this basic technique include the use of a Van Leer type "monotonic limiter" and an additional linear term due to Landshoff which act to keep the artificial diffusion length of the shock front

to a minimum while preventing spurious Gibbs-like oscillations in the vicinity of the shock. We introduce a tensor artificial viscosity by adding an artificial stress tensor $\sigma_a$ to the total stress tensor $\sigma$:

$$\sigma(x) = -p(x)I + \sigma_a(x).$$

We emphasize at this point that the artificial stress (as well as the total stress) is in general a *function* of the spatial coordinates and therefore varies inside a zone.

**6.1. Directional compression measure and artificial stress types.** Traditionally, the tensor artificial stress is defined by one of the two expressions (see [12, 44, 32])

$$\sigma_{a,1} = \mu \nabla v \quad \text{or} \quad \sigma_{a,2} = \mu \varepsilon(v)\,,$$

where $\mu$ is a scalar viscosity coefficient and $\varepsilon(v)$ is the symmetrized velocity gradient

$$\varepsilon(v) \equiv \frac{1}{2}(\nabla v + v\nabla)\,.$$

The coefficient $\mu$ is usually defined in terms of some measure of compression (or velocity jump), for example, the velocity divergence, or velocity derivative in a specific "shock direction." Here, we utilize the latter approach and consider the following *directional measure of compression*: given a direction vector $s$, we set

$$\Delta_s v = \lim_{\alpha\to 0} \frac{v(x+\alpha s) - v(x)}{\alpha |s|} \cdot \frac{s}{|s|} = \frac{\mathrm{d}v}{\mathrm{d}s} \cdot \frac{s}{|s|} = \frac{s \cdot \nabla v \cdot s}{s \cdot s} = \frac{s \cdot \varepsilon(v) \cdot s}{s \cdot s}. \tag{6.1}$$

In other words, the measure of compression is defined by taking the scalar projection (or scalar component) of the velocity $v$ on the vector $s$ and differentiating in the direction of $s$ (using the directional derivative). Note that at any given point $x$, the symmetric tensor $\varepsilon(v)$ is completely characterized by the values of $\Delta_s v$ over all directions $s$. Let us consider a particle $x$ and the line passing through $x$ and parallel to a direction $s$: $L = \{x + \alpha s : \alpha \in \mathbb{R}\}$. From the point of view of an observer moving with the particle $x$ with velocity $v(x)$ the particle $x' = x + \alpha s \in L$ moves with a relative velocity $v_r = v(x') - v(x)$ whose component (or scalar projection) along $s$ is $v_{r,s} = (v(x') - v(x)) \cdot s/|s|$. If this component has the sign of $\alpha$, then the particle $x'$ is moving away from the particle $x$, and conversely, if $v_{r,s}$ has the sign of $-\alpha$, then $x'$ is moving toward $x$. Thus, if $\Delta_s v(x) < 0$, then there is a neighborhood of $x$ along $L$ where all points are moving toward $x$; in other words, $x$ is a *point of compression in the direction* $s$. Similarly, if $\Delta_s v(x) > 0$, then $x$ is a *point of expansion in direction* $s$.

Introduce the spectral decomposition of $\varepsilon(v)$, using tensor product notation,

$$\varepsilon(v) = \sum_k \lambda_k s_k \otimes s_k, \qquad s_i \cdot s_j = \delta_{ij}, \qquad \lambda_1 \le \cdots \le \lambda_d, \tag{6.2}$$

where $\lambda_k$ and $s_k$ are the eigenvalues and eigenvectors, respectively, sorted from smallest to largest eigenvalue. Note that $\Delta_{s_k} v = \lambda_k$ and the identity

$$\min_{|s|=1} \Delta_s v = \min_{|s|=1} s \cdot \varepsilon(v) \cdot s = s_1 \cdot \varepsilon(v) \cdot s_1 = \lambda_1 \tag{6.3}$$

holds, which means that the direction $s_1$ minimizes $\Delta_s v$ over all unit directions $s$ and the measure of compression in direction $s_1$ is given by $\lambda_1$. Thus, $s_1$ is a direction of

TABLE 6.1
*Summary of artificial stress types.*

| Artificial Stress Type | Definition | Symmetric |
|---|---|---|
| Type 1 | $\sigma_a = \mu_{s_1} \nabla v$ | No |
| Type 2 | $\sigma_a = \mu_{s_1}\, \varepsilon(v)$ | Yes |
| Type 3 | $\sigma_a = \mu_{s_1} \lambda_1 s_1 \otimes s_1$ | Yes |
| Type 4 | $\sigma_a = \sum_k \mu_{s_k} \lambda_k s_k \otimes s_k$ | Yes |

maximal compression (or minimal expansion) and therefore it is a natural choice for a shock direction.

Given a unit direction $s$ let us consider the rank-one stress tensor $\sigma = (\mu \Delta_s v)\, s \otimes s$ for some $\mu \geq 0$. The surface force generated by this tensor on a surface with normal vector $n$ is given by $n \cdot \sigma$. Therefore this force will be zero when $n$ is perpendicular to $s$ and equal to $(\mu \Delta_s v) s$ when $n = s$. In the latter case, the direction of this force is such that it resists both compressive and expansive (in the direction $s$) motion. Thus, $\sigma$ is a purely 1D viscous stress. This observation combined with the natural choice of $s_1$ as a shock direction motivates the introduction of the following form of artificial stress:

$$\sigma_{a,3} = \mu \lambda_1 s_1 \otimes s_1 \,.$$

A potential drawback of this form is that it takes into account only a single shock direction and thus does not handle appropriately the interaction of multiple shocks. Note that the symmetric artificial stress $\sigma_{a,2}$ can be written as

$$\sigma_{a,2} = \mu \varepsilon(v) = \sum_k \mu \lambda_k s_k \otimes s_k \,.$$

Both forms $\sigma_{a,2}$ and $\sigma_{a,3}$ can be naturally generalized as

$$\sigma_{a,4} = \sum_k \mu_k \lambda_k s_k \otimes s_k \,,$$

where $\mu_k$ are direction-dependent viscosity coefficients. We can express both $\sigma_{a,2}$ and $\sigma_{a,3}$ in this form, but we can also make a different choice by setting $\mu_k = \mu_{s_k}$, where $\mu_s$ is a direction dependent viscosity coefficient, defined in section 6.2. The motivation for this choice is that $\sigma_{a,4}$ will be very close to $\sigma_{a,3}$ at the front of a single shock wave since in this case there is a single direction of strong compression. At the same time it will handle the interaction of multiple shocks appropriately as it will take into account the multiple directions of strong compression.

We summarize the introduced artificial viscosity types in Table 6.1. For types 1, 2, and 3 we use the directional viscosity coefficient $\mu_s$ in the "shock direction" $s_1$: $\mu = \mu_{s_1}$. Each form of the artificial stress satisfies the inequality

$$\sigma_a(x) : \nabla v(x) \geq 0 \quad \forall x,$$

which is an essential property for ensuring a strictly dissipative artificial viscosity and therefore positive entropy production. The above inequality follows from $\mu_s \geq 0$, the symmetry of $\sigma_{a,2}$, $\sigma_{a,3}$, and $\sigma_{a,4}$ and the equalities

$$\sigma_{a,1} : \nabla v = \mu_{s_1} \nabla v : \nabla v \,, \qquad \sigma_{a,2} : \nabla v = \sigma_{a,2} : \varepsilon(v) = \mu_{s_1} \varepsilon(v) : \varepsilon(v) \,,$$
$$\sigma_{a,3} : \nabla v = \sigma_{a,3} : \varepsilon(v) = \mu_{s_1} \lambda_1^2 \,, \qquad \sigma_{a,4} : \nabla v = \sigma_{a,4} : \varepsilon(v) = \sum_k \mu_{s_k} \lambda_k^2 \,.$$

Note that $\sigma_{a,1}$ is generally not symmetric (unless $\nabla \times v = 0$), which may potentially lead to nonphysical behavior.

Finally, we remark that if we define the symmetric and positive semidefinite tensors

$$\mathrm{M}_2 = \mu_{s_1}\mathrm{I} = \sum_k \mu_{s_1} s_k \otimes s_k\,, \qquad \mathrm{M}_3 = \mu_{s_1} s_1 \otimes s_1\,, \qquad \mathrm{M}_4 = \sum_k \mu_{s_k} s_k \otimes s_k\,,$$

then the artificial viscosity stresses of types 2, 3, and 4 can be equivalently written as

$$\sigma_{a,2} = \mathrm{M}_2 \cdot \varepsilon(v)\,, \qquad \sigma_{a,3} = \mathrm{M}_3 \cdot \varepsilon(v)\,, \qquad \sigma_{a,4} = \mathrm{M}_4 \cdot \varepsilon(v)\,.$$

From this perspective, $\sigma_{a,3}$ and $\sigma_{a,4}$ can be considered generalizations of $\sigma_{a,2}$, where the scalar viscosity coefficient is replaced by a matrix which is diagonal in the local eigenvector basis for $\varepsilon(v)$; cf. [33].

**6.2. Directional viscosity coefficient.** Following [32], we consider a general viscosity coefficient of the form

$$\mu_s(x) \equiv \rho\left\{q_2 \ell_s^2 |\Delta_s v| + q_1 \psi_0 \psi_1 \ell_s c_s\right\}, \tag{6.4}$$

where $q_1$ and $q_2$ are linear and quadratic scaling coefficients, respectively; $\rho$ is the density and $c_s$ is the speed of sound, both evaluated at the point $x$; $\Delta_s v$ is the directional measure of compression from section 6.1; $\ell_s = \ell_s(x)$ is a *directional length scale* defined in the direction of the vector $s$ (see section 6.3) evaluated at the point $x$; and $\psi_1$ is a compression switch which forces the linear term to vanish at points in expansion

$$\psi_1 = \begin{cases} 1, & \Delta_s v < 0, \\ 0, & \Delta_s v \geq 0, \end{cases}$$

and $\psi_0$ is a vorticity switch that suppresses the linear term at points where vorticity dominates the flow

$$\psi_0 = \frac{|\nabla \cdot v|}{\|\nabla v\|}.$$

*Remark* 6.1. A drawback of the above definition of the viscosity coefficient $\mu_s$ is the lack of a "limiter," whose purpose is to make the artificial viscosity negligible in regions where the solution is smooth (as in [12, 32], for example). The definition of such a limiting procedure is not considered here.

**6.3. Directional length scale.** Artificial viscosities require the definition of a grid (mesh) dependent length scale. In many SGH formulations, this length scale is a simple piecewise constant quantity which is computed as the square (cube) root of the zone area (volume). More sophisticated treatments incorporate knowledge of the shock velocity to determine the length scale or define the length scale as more than just a single constant value in the zone (e.g., [12]). Choices made in defining this scale can have significant consequences with regard to the "mesh imprinting" phenomenon that is the bane of many Lagrangian methods.

To match the subzonal nature of our high-order approach we think of the length scale as a function (i.e., a length scale field) defined at a spatial coordinate $x$ in terms of a direction vector $s$, relative to an initial length scale field $\ell_0(\tilde{x})$ on the initial

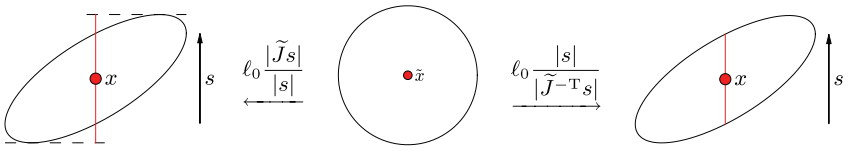


FIG. 6.1. *Examples of the initial length scale field transformation from an initial zone (center) to a Lagrangian zone via* (6.5).

domain $\widetilde{\Omega}$. Specifically, we define $\ell_s(x)$ in terms of the Jacobian $\widetilde{J}$ of the mapping $\widetilde{\Phi} : \widetilde{\Omega} \to \Omega(t)$ from section 2. This allows us to (indirectly) introduce some smoothness in $\ell_s(x)$ by factoring out the effect of the Lagrangian motion.

Consider a circle centered at $\tilde{x} = \widetilde{\Phi}^{-1}(x)$ with diameter $\ell_0(\tilde{x})$. Transforming this circle through the locally linearized mapping

$$\tilde{y} \mapsto y = x + (\tilde{y} - \tilde{x}) \cdot \widetilde{J}(\tilde{x})$$

we obtain an ellipse centered at $x$. One can think of the circle as (a neighborhood in) the initial zone that has been deformed into the ellipse by the Lagrangian motion. Therefore the local length scale $\ell_s(x)$ is defined by measuring the size of the ellipse in the direction $s$. This can be done in two different ways as illustrated by the red line segments in Figure 6.1 corresponding to the formulas

$$\ell_s(x) = \ell_0 \frac{|\widetilde{J}s|}{|s|} \quad \text{and} \quad \ell_s(x) = \ell_0 \frac{|s|}{|\widetilde{J}^{-\mathrm{T}}s|}. \tag{6.5}$$

Our default choice is to use the first definition in (6.5). In practice, the Jacobian matrix $\widetilde{J}$ is computed zone by zone via the zone Jacobians $\mathbf{J}_z$ using (4.6):

$$\widetilde{J}(t) = [\mathbf{J}_z(t_0)]^{-1} \, \mathbf{J}_z(t) \, .$$

Note that the use of the Jacobian of the mapping from the *initial* element in the length scale definition is essential. If we used the mapping from the reference element, or in other words if we used $\mathbf{J}_z(t)$ instead of $\ell_0 \widetilde{J}(t) = \ell_0 \, [\mathbf{J}_z(t_0)]^{-1} \, \mathbf{J}_z(t)$ in (6.5), the symmetry preservation properties of the solution degrade on general grids as illustrated in Figure 6.2.

In practice, the initial length scale field $\ell_0(\tilde{x})$ should be a *smooth* representation of the local mesh size, e.g., the square root of the average zone area (our default option for 2D meshes) or the choice described in section 8.3 specific for 1D problems run on 2D meshes. We also divide $\ell_0$ by the polynomial degree of the kinematic space to provide a proper normalization in the high-order case.

**7. Time integration and the fully discrete approximation.** So far we have focused exclusively on the spatial discretization, but in practice one needs to also discretize the time derivatives in the nonlinear system of ODEs (3.15)–(3.17) obtained after the spatial discretization of the Euler equations. In this section we consider a general high-order temporal discretization method and demonstrate its impact on the semidiscrete conservations laws. Specifically, let $t \in \{t_n\}_{n=0}^{N_t}$, and associate with each moment in time, $t_n$, the computational domain $\Omega^n \equiv \Omega(t_n)$. We identify the quantities of interest defined on $\Omega^n$ with a superscript $n$.

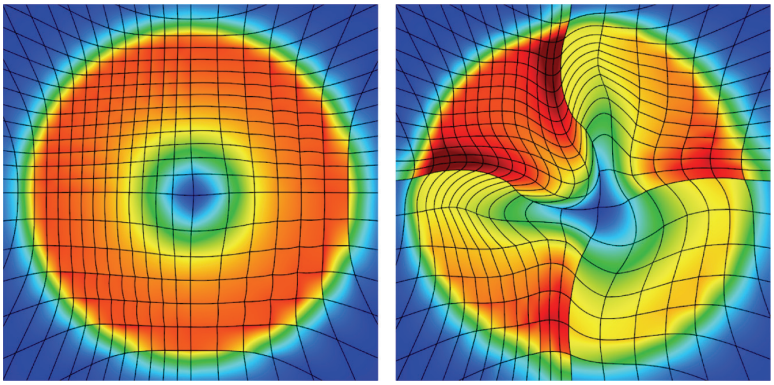

FIG. 6.2. *Numerical results for the Noh implosion problem on a* $24 \times 24$ *distorted grid (cf. section* 8.4*) using the first directional length scale in* (6.5) *defined through a mapping to initial element* $\Omega_z(t_0) \leftarrow \Omega_z(t)$ *(left), versus a mapping to the reference element* $\widehat{\Omega} \leftarrow \Omega_z(t)$ *(right).*

Let $Y = (\mathbf{v}; \mathbf{e}; \mathbf{x})$ be the hydrodynamic state vector. Then the semidiscrete conservation equations of (3.15)–(3.17) can be written in the form

$$\frac{\mathrm{d}Y}{\mathrm{d}t} = \mathcal{F}(Y,t)\,, \qquad \text{where} \qquad \mathcal{F}(Y,t) = \begin{pmatrix} \mathcal{F}_v(\mathbf{v},\mathbf{e},\mathbf{x}) \\ \mathcal{F}_e(\mathbf{v},\mathbf{e},\mathbf{x}) \\ \mathcal{F}_x(\mathbf{v},\mathbf{e},\mathbf{x}) \end{pmatrix} = \begin{pmatrix} -\mathbf{M}_{\mathcal{V}}^{-1}\mathbf{F}\cdot\mathbf{1} \\ \mathbf{M}_{\mathcal{E}}^{-1}\mathbf{F}^{\mathrm{T}}\cdot\mathbf{v} \\ \mathbf{v} \end{pmatrix}.$$

Standard high-order time integration techniques (e.g., explicit Runge–Kutta methods) can be applied to this system of nonlinear ODEs. However, these standard methods may need modifications to ensure numerical stability of the scheme and to ensure exact energy conservation. An example of this is given in the next section.

**7.1. The RK2-average scheme.** The midpoint Runge–Kutta second-order scheme reads

$$Y^{n+\frac{1}{2}} = Y^n + \frac{\Delta t}{2}\,\mathcal{F}(Y^n, t^n)\,, \quad Y^{n+1} = Y^n + \Delta t\,\mathcal{F}(Y^{n+\frac{1}{2}}, t^{n+\frac{1}{2}}).$$

In practice, we have observed that the above scheme may be unstable even for simple test problems. Therefore, we developed a modification of the scheme to improve its stability and to ensure total energy conservation. Its two stages are given by

$$\begin{aligned}
&\mathbf{v}^{n+\frac{1}{2}} = \mathbf{v}^n - (\Delta t/2)\,\mathbf{M}_{\mathcal{V}}^{-1}\mathbf{F}^n\cdot\mathbf{1}, && \mathbf{v}^{n+1} = \mathbf{v}^n - \Delta t\,\mathbf{M}_{\mathcal{V}}^{-1}\mathbf{F}^{n+\frac{1}{2}}\cdot\mathbf{1}, \\
&\mathbf{e}^{n+\frac{1}{2}} = \mathbf{e}^n + (\Delta t/2)\,\mathbf{M}_{\mathcal{E}}^{-1}(\mathbf{F}^n)^{\mathrm{T}}\cdot\mathbf{v}^{n+\frac{1}{2}}, && \mathbf{e}^{n+1} = \mathbf{e}^n + \Delta t\,\mathbf{M}_{\mathcal{E}}^{-1}(\mathbf{F}^{n+\frac{1}{2}})^{\mathrm{T}}\cdot\bar{\mathbf{v}}^{n+\frac{1}{2}}, \\
&\mathbf{x}^{n+\frac{1}{2}} = \mathbf{x}^n + (\Delta, t/2)\,\mathbf{v}^{n+\frac{1}{2}}, && \mathbf{x}^{n+1} = \mathbf{x}^n + \Delta t\,\bar{\mathbf{v}}^{n+\frac{1}{2}},
\end{aligned}$$

where $\mathbf{F}^k = \mathbf{F}(Y^k)$ and $\bar{\mathbf{v}}^{n+\frac{1}{2}} = (\mathbf{v}^n + \mathbf{v}^{n+1})/2$.

PROPOSITION 7.1. *The RK*2*-average scheme described above conserves the discrete total energy exactly.*

*Proof.* The change in kinetic (KE) and internal (IE) energy can be expressed as

$$\begin{aligned}
KE^{n+1} - KE^n &= (\mathbf{v}^{n+1} - \mathbf{v}^n)\cdot\mathbf{M}_{\mathcal{V}}\cdot\bar{\mathbf{v}}^{n+\frac{1}{2}} = -\Delta t\,(\mathbf{F}^{n+\frac{1}{2}}\cdot\mathbf{1})\cdot\bar{\mathbf{v}}^{n+\frac{1}{2}} \\
IE^{n+1} - IE^n &= \mathbf{1}\cdot\mathbf{M}_{\mathcal{E}}\cdot(\mathbf{e}^{n+1} - \mathbf{e}^n) = \Delta t\,\mathbf{1}\cdot(\mathbf{F}^{n+\frac{1}{2}})^{\mathrm{T}}\cdot\bar{\mathbf{v}}^{n+\frac{1}{2}})\,.
\end{aligned}$$

Therefore the discrete total energy is preserved: $KE^{n+1} + IE^{n+1} = KE^n + IE^n$. ∎

**7.2. Higher-order methods.** We have also tested higher-order time discretization methods like the strong stability preserving (SSP) RK3 scheme [28], and the classical RK4 scheme. In our experience, they do not have the instability issues observed for the midpoint RK2 scheme (also observed for the SSP RK2 method, also known as Heun's method). A drawback of these schemes is that they do not preserve the total energy exactly. However, since they give high-order temporal approximations to the semidiscrete method, which preserves the total energy, the error in the total energy is of higher order at least for smooth problems.

**7.3. Automatic time-step control.** To facilitate automatic time-step control, we define a time-step estimate $\tau^n$ as the minimum (over all quadrature points used in the evaluation of the local force matrices $\mathbf{F}_z$) of the expression

$$\tau^n = \min_x \ \alpha \left( \frac{c_s(x)}{h_{\min}(x)} + \alpha_\mu \frac{\mu_s(x)}{\rho(x) h_{\min}^2(x)} \right)^{-1},$$

where $h_{\min}(x)$ is the minimal singular value of $\mathbf{J}_z(\hat{x})$ (divided by the kinematic space degree for high-order methods) and $\alpha, \alpha_\mu$ are given CFL constants, which typically we define as $\alpha = 0.5$ and $\alpha_\mu = 2.5$. In multistage time-stepping methods, $\tau^n$ is taken to be the minimum over all stages. With this definition of $\tau^n$, we use the following algorithm to control the time-step:

1. Given a time-step $\Delta t$ and state $Y^n$, evaluate the state $Y^{n+1}$ and the corresponding time-step estimate $\tau^n$.
2. If $\Delta t \geq \tau^n$, set $\Delta t = \beta_1 \Delta t$ and go to step 1.
3. If $\Delta t \leq \gamma \tau^n$, set $\Delta t = \beta_2 \Delta t$.
4. Set $n = n + 1$ and continue with the next time-step.

Here, $\beta_1$, $\beta_2$, and $\gamma$ denote given constants. The default values we use are $\beta_1 = 0.85$, $\beta_2 = 1.02$, and $\gamma = 0.8$.

**8. Numerical results.** We now present a series of numerical results using a set of high-order methods corresponding to specific choices for the finite element spaces describing the kinematic variables of position $x$ and velocity $v$, and the thermodynamic variable $e$. We designate each method using the notation $Q_k$-$Q_{k-1}$ (for quadrilateral or hexahedral meshes) as described in section 4.7. Our goal in this section is not to provide an exhaustive study of the effects of choices for basis function order or the type of artificial viscosities from Table 6.1 (which we believe is the subject of a different paper), but rather to demonstrate the general features that high-order curvilinear methods have in the context of classical Lagrangian hydrodynamics benchmarks. For all test cases considered, we solve the global linear system for momentum conservation using a diagonally scaled conjugate gradient algorithm to a residual tolerance of $10^{-8}$, and unless otherwise specified, we use an ideal gas equation of state with a constant adiabatic index $\gamma = 5/3$. For the shock wave test problems, unless otherwise specified, we use the type 2 artificial viscosity from Table 6.1 (our default choice) with the length scale defined by the left side of (6.5), constant $\ell_0$, and coefficients $q_1 = 1/2$ and $q_2 = 2$. The results in this section have been computed with our high-order finite element Lagrangian hydrocode BLAST [6], which is based on the parallel modular FEMs library MFEM [41]. We also used the related OpenGL visualization tool GLVis [27] to plot the computed curvilinear meshes and high-order fields.

**8.1. 2D Taylo–Green vortex.** The purpose of this example is to verify the ability of our fully discrete methods to obtain high-order convergence in time and space on a moving mesh with nontrivial deformation for the case of a smooth (shock-free)

problem. Here we consider a simple, steady state solution to the 2D incompressible, inviscid Navier–Stokes equations, given by the initial conditions

$$v = \left\{ \sin(\pi x)\cos(\pi y), -\cos(\pi x)\sin(\pi y) \right\}, \qquad p = \frac{\rho}{4}(\cos(2\pi x) + \cos(2\pi y)) + 1\,.$$

We can extend this incompressible solution to the compressible case with an ideal gas equation of state and constant adiabatic index $\gamma = 5/3$ by using a manufactured solution, meaning that we assume these initial conditions are steady state solutions to the Euler equations, then we solve for the resulting source terms and use these to drive the time-dependent simulation. The flow is incompressible ($\nabla \cdot v = 0$) so the density field is constant in space and time and we use $\rho \equiv 1$. It is easy to check that $\rho\frac{dv}{dt} = -\nabla p$ so the external body force is zero. In the energy equation, using $e = p/((\gamma - 1)\rho)$, we compute

$$e_{\text{src}} = \rho\frac{de}{dt} + p\nabla \cdot v = \frac{de}{dt} = \frac{3\pi}{8}\left(\cos(3\pi x)\cos(\pi y) - \cos(\pi x)\cos(3\pi y)\right).$$

This procedure allows us to run the time-dependent problem to some point in time, then perform normed error analysis on the final computational mesh using the exact solutions for $v$ and $p$. The computational domain is a unit box with wall boundary conditions on all surfaces ($v \cdot n = 0$). Note that for this manufactured solution all fields are steady state, i.e., they are independent of time; however, they do vary along particle trajectories and with respect to the computational mesh as it moves. We run the problem to $t = 0.75$. Since this problem is smooth we run without any artificial viscosity and do normed error analysis on the solution at the final time and compute convergence rates using a variety of high-order methods.

In Figure 8.1 we show plots of the (curvilinear) mesh and velocity field magnitude at times $t = 0$ and $t = 0.75$ using three different mesh-method combinations. The first case we consider is a $Q_2$-$Q_1$ method on an initially structured quadrilateral mesh using the energy conserving second-order RK2-average time integration method presented in section 7; the second case is a $P_3$-$P_2$ method on a triangular mesh (obtained by subdividing each zone of the previous quadrilateral mesh along its diagonal) using a third-order strong stability preserving time integration method (RK3SSP) [28]; and the final case is a $Q_4$-$Q_3$ method on an initially unstructured quadrilateral mesh using a fourth-order time integration method (RK4). Note the degree to which each mesh is distorted as well as the curvilinear element boundaries in each case and compare to the exact motion of Figure 4.2. In Figure 8.2 we plot error convergence (using the $L_2$ norm) of the velocity field at the final time $t = 0.75$ for each case considered on a sequence of four successively refined meshes. Note that for each case we observe the expected (high-order) convergence rates of second-, third-, and fourth-order, even on the highly deformed curvilinear mesh.

**8.2. 2D single material, single-mode Rayleigh–Taylor instability.** The purpose of this example is to demonstrate the ability of high-order curvilinear methods to better resolve complex flow features and achieve greater robustness in a moving Lagrangian mesh when compared to low-order methods on a refined mesh (with the same number of degrees of freedom). Here we consider a variation of the classic Rayleigh–Taylor instability problem [2] which consists of a heavy fluid resting on top of a light fluid in a gravitational field supported by a counterbalancing pressure gradient. The problem domain considered is $(x, y) \in [0, L/2] \times [-L, L]$ with symmetry planes at $x = 0$ and $x = L/2$, where $L = 1$. Initially, we have $\frac{dp}{dy} = \rho g$ with $p(x, L) = 4$ and

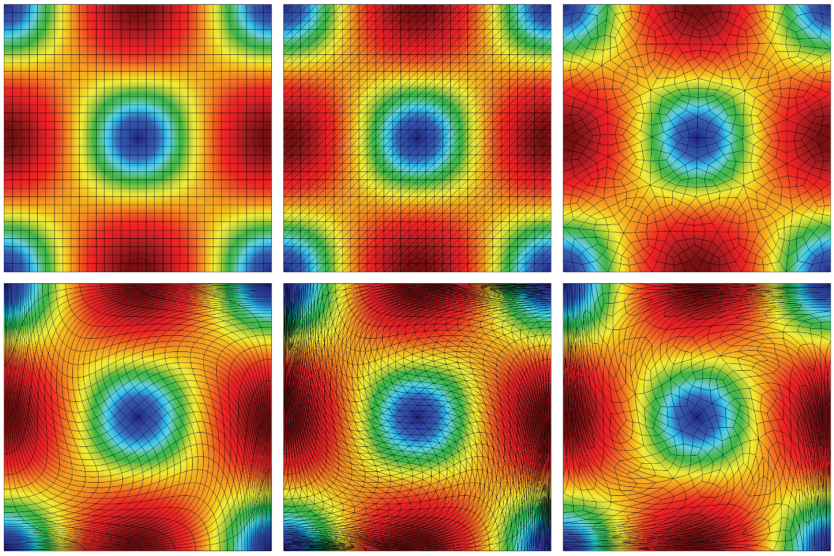

FIG. 8.1. *Initial ($t = 0$, top row) and final ($t = 0.75$, bottom row) curvilinear mesh and velocity field magnitudes for the 2D Taylor–Green vortex problem using three different combinations of meshes and high-order methods: $Q_2$-$Q_1$ (left), $P_3$-$P_2$ (middle), and $Q_4$-$Q_3$ (right).*

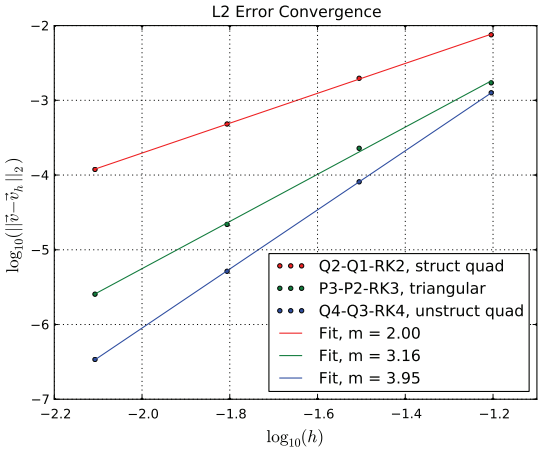


FIG. 8.2. *Error convergence in velocity field using the $L_2$ norm for the 2D Taylor–Green vortex problem using three different combinations of meshes and high-order methods.*

the "gravitational" constant $g = -1$. For this problem, a purely Lagrangian method precludes the use of a two-material state separated by a contact discontinuity since the flow will form a "slide" surface with discontinuous velocities at the interface. We therefore consider the case of a single material with an initial smooth density gradient in the vertical (or $y$) direction given by

$$\rho(y) = \frac{\rho_1 + \rho_2}{2} + \frac{\rho_2 - \rho_1}{\pi} \arctan(\beta y),$$

where $\rho_1 = 1$, which represents the "light" material, $\rho_2 = 2$, which represents the "heavy" material, and the smoothing parameter $\beta = 20$. To set up the hydrodynamic

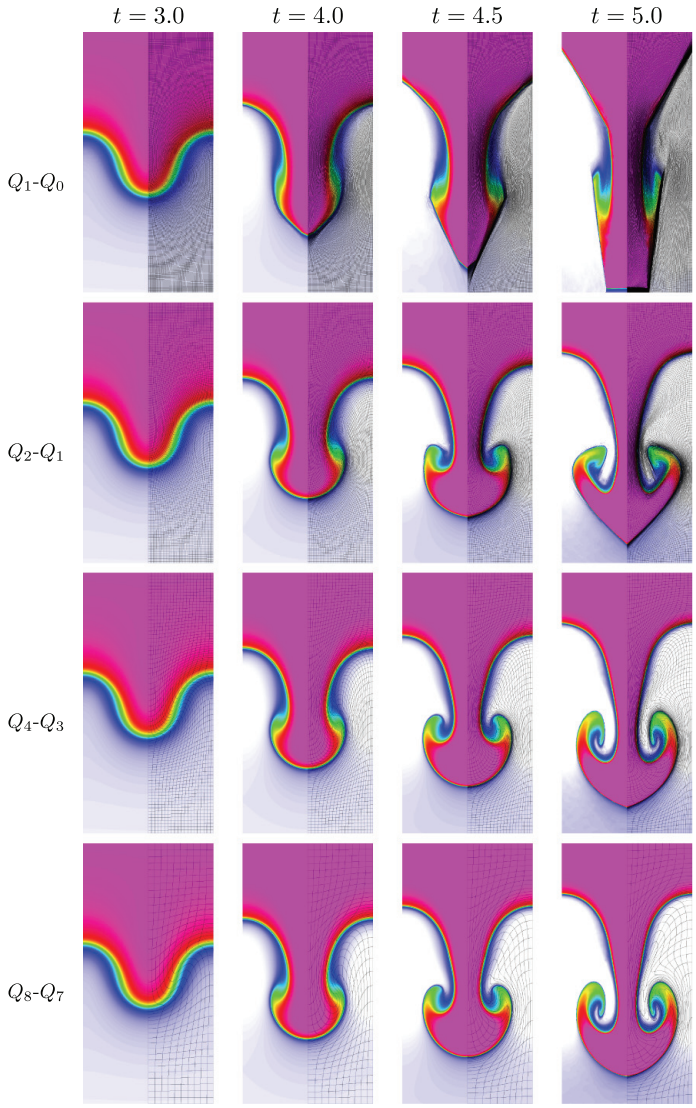


FIG. 8.3. *Snapshots in time corresponding to* $t = 3.0$, $t = 4.0$, $t = 4.5$, *and* $t = 5.0$ *for the single-material, single-mode Rayleigh–Taylor instability problem using a sequence of high-order methods with the same number of degrees of freedom.*

instability across the initial density gradient, we apply an initial divergence-free velocity perturbation to the whole problem given by

$$v = v_0 \exp(-2\pi y^2)\Big\{2y \sin(2\pi x), \cos(2\pi x)\Big\} \qquad \text{with } v_0 = 0.02\,.$$

As with the previous problem, this problem is smooth and we therefore run without any artificial viscosity.

In Figure 8.3 we show plots of the (curvilinear) mesh and density field at different snapshots in time corresponding to $t = 3.0$, $t = 4.0$, $t = 4.5$, and $t = 5.0$ for the case of four different high-order curvilinear methods: $Q_1$-$Q_0$ (analogous to traditional

SGH), $Q_2$-$Q_1$, $Q_4$-$Q_3$ and $Q_8$-$Q_7$. In each case, the total number of kinematic and thermodynamic degrees of freedom is held constant. This is achieved by derefining the mesh one level for every doubling of the spatial order of the method used. Note that as time increases and the problem develops more vorticity, the low-order methods begin to lock up and are no longer able to resolve the flow as the mesh begins to tangle. As the order of the method is increased, the problem is able to run further in time and resolve more of the flow features while maintaining robustness in the Lagrangian mesh.

**8.3. 1D Sod shock tube.** We now transition to shock wave problems which require the use of artificial viscosity for shock capturing. The purpose of this example is to verify the ability of our high-order methods to propagate shocks, rarefaction waves, and contact discontinuities in one dimension. We consider a simple 1D Riemann problem, the Sod shock tube, on the domain $x \in [0, 1]$ consisting of two materials with different initial states denoted L (left) and R (right), separated by a contact discontinuity at $x = 0.5$. Results on this benchmark using a $Q_2$-$Q_1$ method have been reported in [22]; here we compare the same problem using a $Q_8$-$Q_7$ method with an identical number of degrees of freedom and use artificial viscosity type 4 from Table 6.1.

In Figure 8.4 we show scatter plots of the velocity, density, internal energy, and pressure versus the $x$-coordinate at the final time of $t = 0.2$ and compare it to the analytic solution using both a $Q_8$-$Q_7$ method on a 1D 50-zone mesh (consisting of 50 zones in the $x$ direction and a single zone in the $y$ direction with $y \in [0, 0.1]$) and a

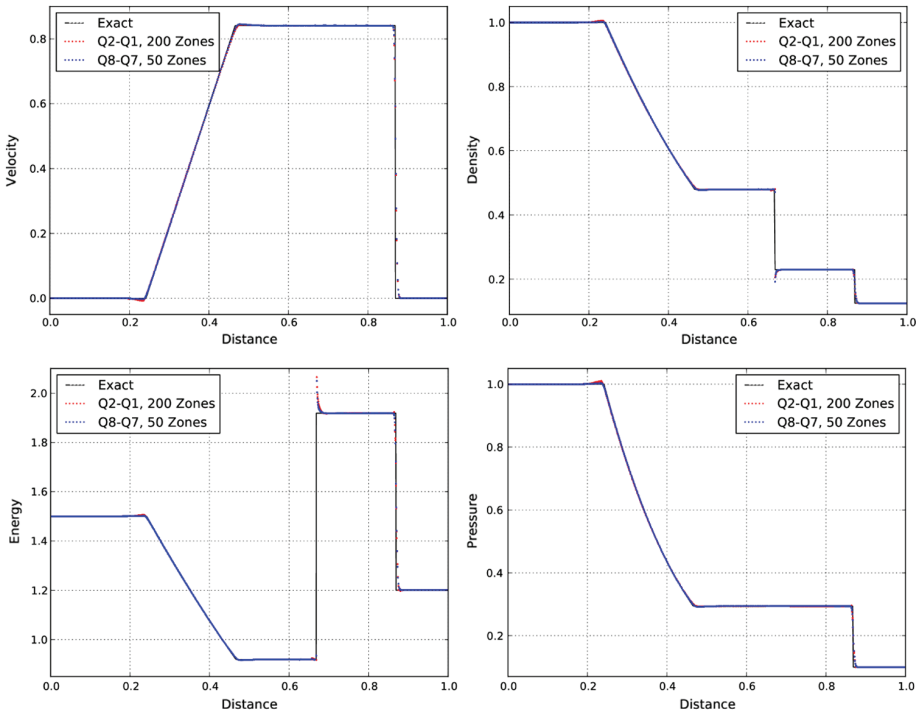


FIG. 8.4. *Results for the Sod shock tube on a* 200*-zone mesh using a* $Q_2$-$Q_1$ *method and a* 50*-zone mesh using a* $Q_8$-$Q_7$ *method: velocity (top left), density (top right), internal energy (bottom left) and pressure (bottom right).*

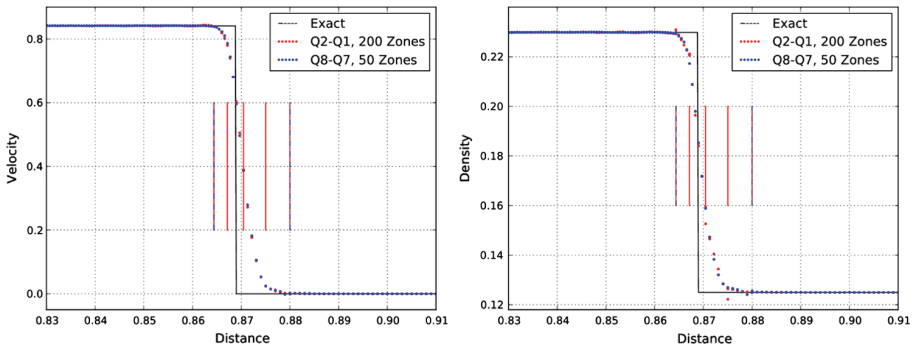


FIG. 8.5. *Results for the Sod shock tube on a* 200*-zone mesh using a* $Q_2$*-*$Q_1$ *method and a* 50*-zone mesh using a* $Q_8$*-*$Q_7$ *method, zoomed in around the shock front illustrating the high-order continuous velocity (left) and discontinuous density (right). The zone boundaries around the shock are designated with color-coded vertical lines.*

$Q_2$-$Q_1$ method on a twice-refined version of the same mesh. For this 1D problem, the initial length scale $\ell_0$ is defined using the zone size in the $x$ direction divided by the order of the kinematic space, so that $\ell_0 \equiv 1/400$ for both $Q_2$-$Q_1$ and $Q_8$-$Q_7$ methods. For each plot, the fields are sampled using the underlying high-order finite element basis function representation with 25 plot points per zone (5 in the $x$-direction) for the $Q_2$-$Q_1$ method and 400 plot points per zone (20 in the $x$-direction) for the $Q_8$-$Q_7$ method. The sampling of the solutions at the subzone level is essential to resolve the high-order data that is present in the solution. In both cases we capture the material contact discontinuity without any diffusion (since we are using a discontinuous internal energy basis), and in both cases we observe the "wall heating" phenomenon in the internal energy and its subsequent effect on the density at the contact. Furthermore, we can conclude for both cases that the ability to resolve the rarefaction wave is evidence that our artificial viscosity is not excessively damping the solution in smooth regions. Note that the low-order method on the fine mesh yields essentially the same result as the high-order method on the coarse mesh.

In Figure 8.5 we show plots of the velocity and density zoomed in around the shock front. In addition, we designate with color-coded vertical lines the zone boundary around the shock for the $Q_8$-$Q_7$ method and the corresponding four refined zones for the $Q_2$-$Q_1$ method. Here we can more clearly see the high-order, subzonal variation in both the continuous velocity and piecewise discontinuous density. For the $Q_8$-$Q_7$ method, the shock is entirely resolved in a single zone. Note that even though we are using an eighth-order polynomial basis for the velocity and a seventh-order polynomial basis for the internal energy for $Q_8$-$Q_7$ method, we do not observe spurious oscillations at the shock front.

**8.4. 2D Sedov explosion and Noh implosion on a nonuniform mesh.** The purpose of these examples is to demonstrate the benefits of our high-order artificial viscosity formulation in maintaining symmetry for shock wave propagation over irregular meshes. Here we consider the standard shock hydrodynamic benchmarks of the Sedov explosion [46] and the Noh implosion [42] test problems in planar $x$-$y$ geometry on a nonstandard Cartesian mesh of the domain $(x, y) \in [-L, L] \times [-L, L]$ with $16 \times 16$ zones in the quadrant $(x, y) \in [0, L] \times [-L, 0]$, $32 \times 32$ zones in the quadrant $(x, y) \in [-L, 0] \times [0, L]$, $16 \times 32$ zones in the quadrant $(x, y) \in [-L, 0] \times [-L, 0]$, and $32 \times 16$ zones in the quadrant $(x, y) \in [0, L] \times [0, L]$. Maintaining

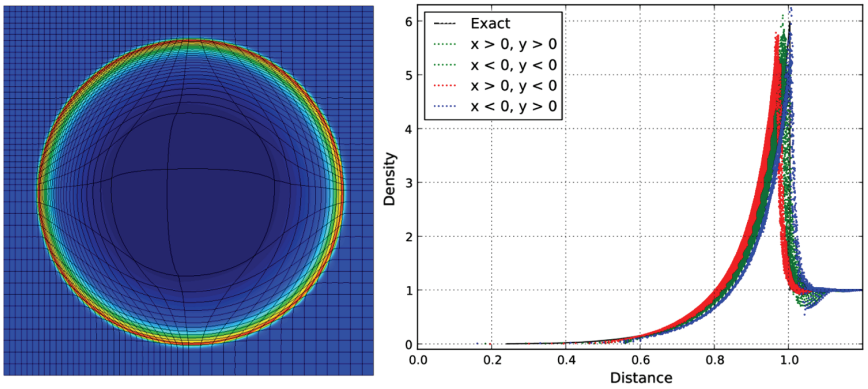


FIG. 8.6. *Density field and curvilinear mesh (left) and scatter plot of density vs. radius colored by quadrant (right) for the Sedov problem on a Cartesian grid with different mesh spacing in different quadrants using a $Q_2$-$Q_1$ method.*

radial symmetry for these test problems on such a mesh with a Lagrangian method is a nontrivial task.

The Sedov problem consists of an ideal gas ($\gamma = 1.4$) with a delta function source of internal energy deposited at the origin such that the total energy $E_{tot} = 1$. The sudden release of the energy creates an expanding shock wave, converting the initial internal energy into kinetic energy. The delta function energy source is approximated by setting the internal energy $e$ to zero in all degrees of freedom except at the origin where the value is chosen so that the total internal energy is 1. In Figure 8.6 we show plots of the density field and curvilinear mesh ($L = 1.2$) at the final time of $t = 1.0$ as well as scatter plots of density versus radius sampled at 25 points per zone for the case of a $Q_2$-$Q_1$ method. Note that even though the shock wave is crossing regions of the mesh with disparate resolutions and aspect ratios, its radial nature is preserved.

The Noh problem consists of an ideal gas with $\gamma = 5/3$, initial density $\rho_0 = 1$, and initial energy $e_0 = 0$. The value of each velocity degree of freedom is initialized to a radial vector pointing toward the origin, $v = -\vec{r}/\|\vec{r}\|$. The initial velocity generates a stagnation shock wave that propagates radially outward and produces a peak post-shock density of $\rho = 16$. In Figure 8.7 we show plots of the density field and curvilinear mesh ($L = 1.0$) at the final time of $t = 0.6$ as well as scatter plots of density versus radius sampled at 25 points per zone for the case of a $Q_2$-$Q_1$ method. As before, note that the stagnation shock front remains largely radial.

**8.5. 2D multimaterial shock triple point interaction.** The purpose of this example is to demonstrate that the results from section 8.2 carry over to multi-material shock driven problems as well. Here we consider a three-state, two-material, 2D Riemann problem which generates vorticity (see [26] for detailed description). For a Lagrangian method, there is a limit to how long this problem can be run due to the generation of vorticity. Here we demonstrate the advantage that high-order curvilinear methods can provide in this context. In this example we use the type 4 artificial viscosity from Table 6.1 and the coefficients $q_1 = 1/4$ and $q_2 = 2/3$. We note that this problem will also run with our default choices; we make the modifications here to demonstrate that even with lower amounts of artificial viscosity, the high-order methods are still capable of robust performance.

In Figure 8.8 we show plots of the (curvilinear) mesh and density field (log scale) at time $t = 3.3$ for the case of three different high-order curvilinear methods: $Q_2$-$Q_1$,

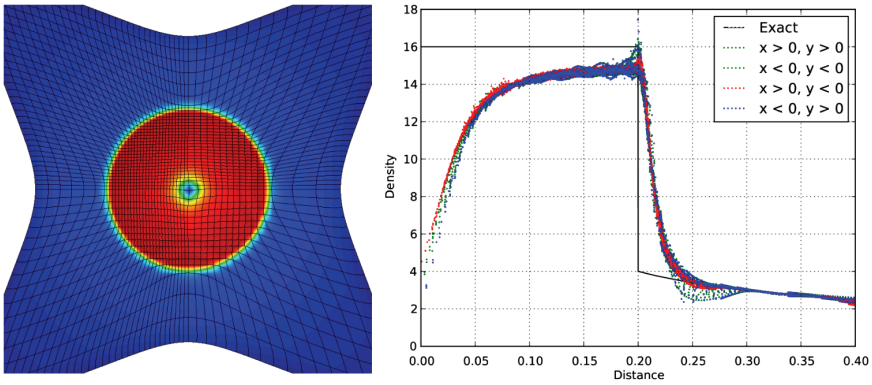


FIG. 8.7. *Density field and curvilinear mesh (left) and scatter plot of density vs. radius colored by quadrant (right) for the Sedov problem on a Cartesian grid with different mesh spacing in different quadrants using a $Q_2$-$Q_1$ method.*

$Q_4$-$Q_3$, and $Q_8$-$Q_7$. As in previous examples, the total number of kinematic and thermodynamic degrees of freedom is held constant by de-refining the mesh one level for every doubling of the spatial order of the method used. Note that for each case, the shock locations are essentially identical, but the total amount of "roll-up" at the triple point increases as the order of the spatial approximation increases. Note also that since these are purely Lagrangian calculations, the material interfaces are preserved in contrast to ALE calculations of this problem (e.g., in [26]) which either diffuse the interface or require interface reconstruction.

**8.6. 3D multimaterial spherical implosion.** The purpose of this example is to demonstrate the benefits of high-order curvilinear methods with respect to symmetry preservation in 3D problems. Maintaining spherical symmetry on 3D unstructured meshes remains a major challenge for most Lagrangian (or ALE) schemes. Here we consider a simple 1D multimaterial implosion problem on an unstructured 3D mesh. The problem consists of a low-density material with $\rho_1 = 0.05$ in the radial range $r \in [0, 1]$ surrounded by a shell of high density material $\rho_2 = 1.0$ in the radial range $r \in [1.0, 1.2]$. Each material is at an initial pressure of $p = 0.1$ and uses an ideal gas equation of state with $\gamma = 5/3$. This problem was originally proposed by [26] for cylindrical symmetry. Here we make a simple modification for spherical symmetry; instead of applying a time-dependent pressure source to the outermost radial surface of the problem, we apply a constant velocity source of $v = -5\vec{r}/\|\vec{r}\|$.

The outer surface drives a spherical shock wave inward. Ideally, the interface between the high- and low-density materials should remain perfectly spherical for all time due to the spherical symmetry of the velocity drive. However, the discretization errors of the initial geometry of this surface and subsequent error introduced by the numerical algorithm will be amplified over time since the interface is subject to both Richtmyer–Meshkov and Rayleigh–Taylor instabilities. In Figure 8.9 we show plots of the mesh and density on a log scale at three snapshots in time using a $Q_1$-$Q_0$ method. In Figure 8.10 and Figure 8.11 we show the same plots using high-order $Q_2$-$Q_1$ and $Q_4$-$Q_3$ methods on curvilinear meshes that are de-refined so that each of the three cases has an identical number of kinematic and thermodynamic degrees of freedom. Note the curved initial geometry for the two high-order cases. (All high-order position degrees of freedom are mapped to spherical surfaces in the outer high-density shell.)

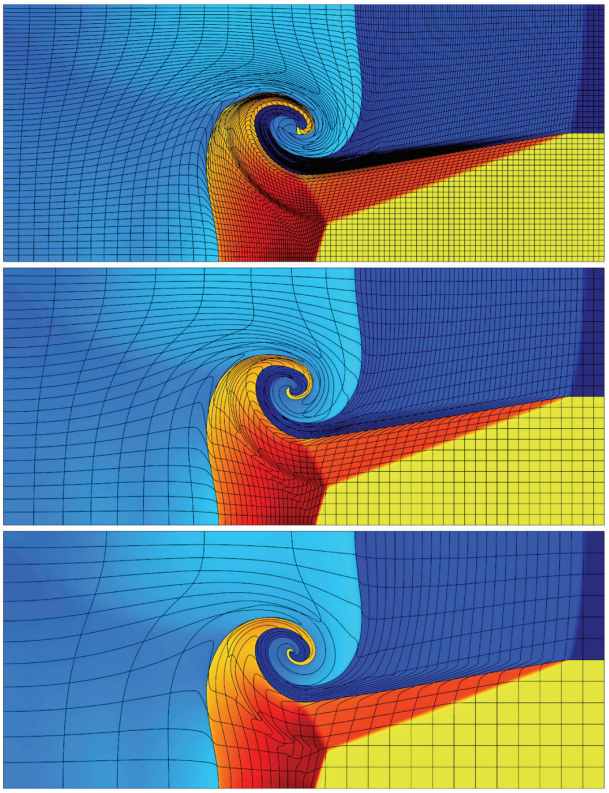

FIG. 8.8. *Density field (log scale) and curvilinear mesh for the 2D multimaterial shock triple-point problem at time $t = 3.3$ using $Q_2$-$Q_1$ (top), $Q_4$-$Q_3$ (middle), and $Q_8$-$Q_7$ (bottom) methods with the same number of degrees of freedom.*

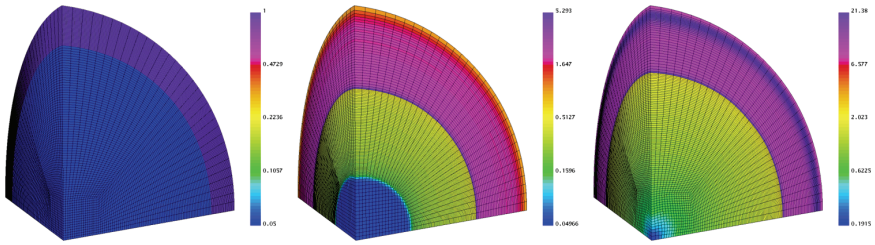

FIG. 8.9. *Snapshots of mesh and density (log scale) at times $t = 0$, $t = 0.08$ and $t = 0.15$ for the 3D multimaterial spherical implosion problem using a $Q_1$-$Q_0$ method.*

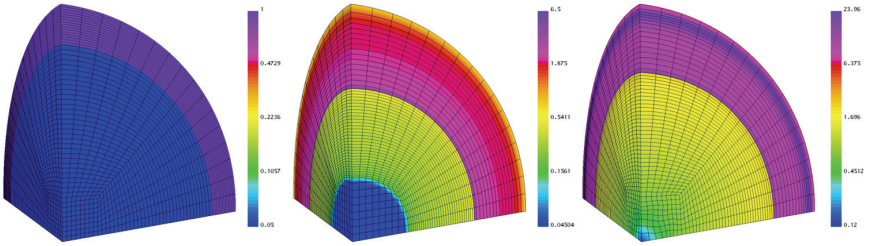

FIG. 8.10. *Snapshots of mesh and density (log scale) at times $t = 0$, $t = 0.08$ and $t = 0.15$ for the 3D multimaterial spherical implosion problem using a $Q_2$-$Q_1$ method.*

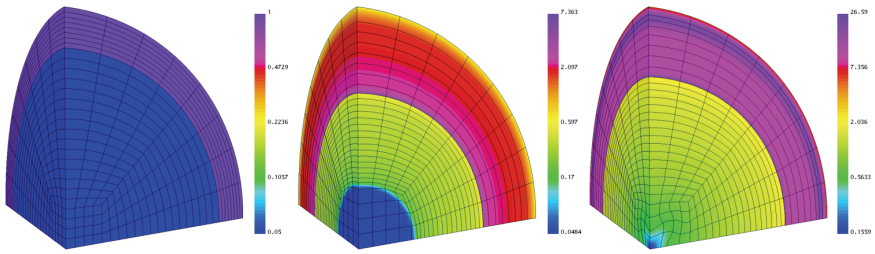

FIG. 8.11. *Snapshots of mesh and density (log scale) at times $t = 0$, $t = 0.08$ and $t = 0.15$ for the 3D multimaterial spherical implosion problem using a $Q_4$-$Q_3$ method.*

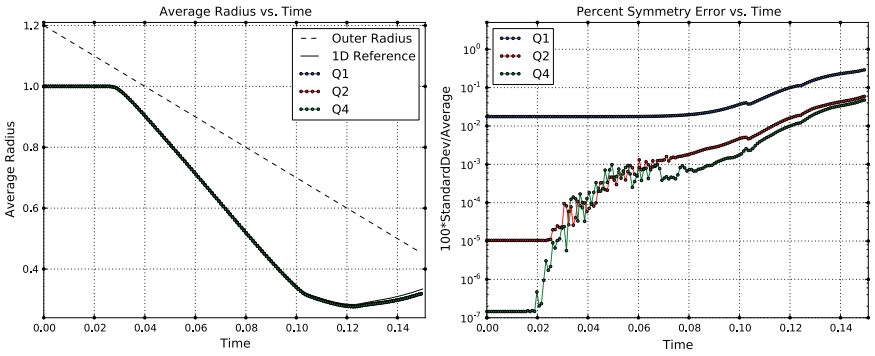


FIG. 8.12. *Average interface radius vs. time (left) and percent symmetry error vs. time (right) for the 3D multimaterial spherical implosion problem using a sequence of high-order methods with a fixed number of degrees of freedom for each case.*

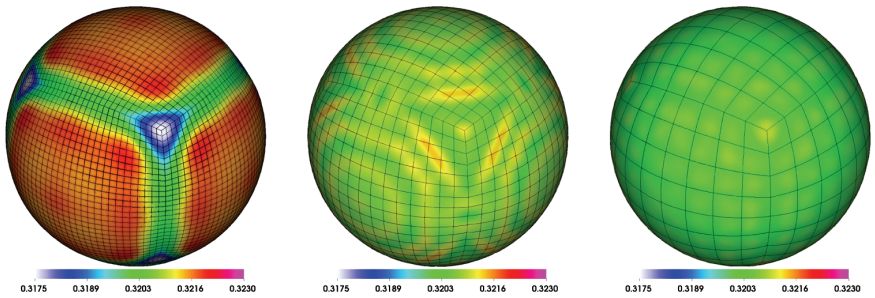

FIG. 8.13. *Plots of interface radius (reflected into a full sphere for visual clarity) using a fixed color scale for the 3D multimaterial spherical implosion problem at time $t = 0.15$ using a $Q_1$-$Q_0$ method (left), a $Q_2$-$Q_1$ method (center), and a $Q_4$-$Q_3$ method (right).*

Note also the 3D subzonal resolution of the inwardly moving shock at $t = 0.8$ for the $Q_4$-$Q_3$ case.

In Figure 8.12 we plot the average radius of the entire material interface (surface) sampled at 9 points per face for the $Q_1$-$Q_0$ method, 25 points per face for the $Q_2$-$Q_1$ method, and 81 points per face for the $Q_4$-$Q_3$ method (resulting in the same total number of interface sample points for each case) and compare this to a reference 1D result (obtained from a high resolution 1D Lagrangian SGH calculation). Note that all three methods achieve essentially identical results in the average radius. In Figure 8.12 we also plot the normalized standard deviation of this radial surface which indicates

the symmetry error over time. When computing spatial errors using a traditional SGH code, the error is usually only considered at the mesh vertices (i.e., 4 points per face). Here we are sampling the symmetry error at 9 points per face for the $Q_1$-$Q_0$ method to emphasize the "faceting" error that is introduced by approximating the spherical surface using bilinear face patches. As indicated in Figure 8.12, the $Q_2$-$Q_1$ and $Q_4$-$Q_3$ methods are much better at approximating the initial spherical geometry and at preserving the time evolved symmetry of the interface for a fixed number of degrees of freedom. This is demonstrated further in Figure 8.13, where we show surface plots of the calculated radius at the final time of $t = 0.15$ for all three cases.

**9. Conclusions.** In this paper we presented a high-order curvilinear FEM for solving the equations of compressible hydrodynamics in a Lagrangian frame. This approach is general with respect to the choice of kinematic and thermodynamic bases and can be considered a high-order generalization of classical methods. We demonstrated via numerical examples a number of practical benefits, including the ability to more accurately capture the geometry of the flow and maintain robustness with respect to mesh motion using curvilinear zones; significant improvements in symmetry preservation for symmetric flows; the elimination of the need for ad hoc hourglass filters; and sharper resolution of a shock front for a given mesh resolution including the ability to represent a shock within a single zone. Our approach capitalizes on several new tools in the context of computational hydrodynamics, such as the *functional point of view* regarding the approximation of field variables and mesh geometry, the concept of *strong mass conservation*, the *artificial viscosity length scale* defined with respect to the initial mesh, and the use of *curvilinear zones* to more accurately model initial and time evolving geometries. We plan to extend our general finite element discretization framework, and these tools in particular, to also address problems with axial symmetry, and elastic-plastic deformation models, as well as the remesh and remap steps in the overall ALE framework.

## REFERENCES


[1] A. Barlow, *A compatible finite element multi-material ALE hydrodynamics algorithm*, Internat. J. Numer. Methods Fluids, 56 (2007), pp. 953–964.

[2] A. Barlow, *private communication*, 2010.

[3] A. L. Bauer, D. E. Burton, E. J. Caramana, R. Loubère, M. J. Shashkov, and P. P. Whalen, *The internal consistency, stability, and accuracy of the discrete, compatible formulation of Lagrangian hydrodynamics*, J. Comput. Phys., 218 (2006), pp. 572–593.

[4] D. J. Benson, *An efficient, accurate, and simple ALE method for nonlinear finite element programs*, Comput. Methods Appl. Mech. Engrg., 72 (1989), pp. 305–350.

[5] D. J. Benson, *Computational methods in Lagrangian and Eulerian hydrocodes*, Comput. Methods Appl. Mech. Engrg., 99 (1992), pp. 235–394.

[6] *BLAST: High-Order Finite Element Lagrangian Hydrocode*, http://www.llnl.gov/CASC/blast.

[7] B. Boutin, E. Deriaz, P. Hoch, and P. Navaro, *Extension of ALE methodology to unstructured conical meshes*, ESAIM Proc., 32 (2011), pp. 31–55.

[8] D. Braess, *Finite Elements: Theory, Fast Solvers, and Applications in Solid Mechanics*, 2nd ed., Cambridge University Press, New York, 2001.

[9] S. C. Brenner and L. R. Scott, *The Mathematical Theory of Finite Element Methods*, Texts in Appl. Math. 15, Springer, New York, 2002.

[10] D. E. Burton, *Multidimensional Discretizations of Conservation Laws for Unstructured Polyhedral grids*, Tech. rep. UCRL-JC-118306, Lawrence Livermore National Laboratory, 1994.

[11] J. C. Campbell, J. M. Hyman, and M. J. Shashkov, *Mimetic finite differecne operators for second-order tensors on unstructured grids*, Comput. Math. Appl., 44 (2002), pp. 157–173.

[12] J. C. Campbell and M. J. Shashkov, *A tensor artificial viscosity using a mimetic finite difference algorithm*, J. Comput. Phys., 172 (2001), pp. 739–765.

[13] E. J. Caramana, D. E. Burton, M. J. Shashkov, and P. P. Whalen, *The construction of compatible hydrodynamics algorithms utilizing conservation of total energy*, J. Comput. Phys., 146 (1998), pp. 227–262.
[14] E. J. Caramana and M. J. Shashkov, *Elimination of artificial grid distortion and hourglass-type motions by means of Lagrangian subzonal masses and pressures*, J. Comput. Phys., 142 (1998), pp. 521–561.
[15] E. J. Caramana, M. J. Shashkov, and P. P. Whalen, *Formulations of artificial viscosity for multi-dimensional shock wave computations*, J. Comput. Phys., 144 (1998), pp. 70–97.
[16] J. Cheng and C.-W. Shu, *A third order conservative lagrangian type scheme on curvilinear meshes for the compressible euler equations*, Commun. Comput. Phys., 4 (2008), pp. 1008–1024.
[17] R. B. Christensen, *Godunov Methods on a Staggered Mesh: An Improved Artificial Viscosity*, Tech. rep. UCRL-JC-105269, Lawrence Livermore National Laboratory, 1991.
[18] P. G. Ciarlet, *The Finite Element Method for Elliptic Problems*, North-Holland, Dordrecht, Netherlands, 1978.
[19] J. Cottrell, T. Hughes, and Y. Bazilevs, *Isogeometric Analysis: Toward Integration of CAD and FEA*, Wiley, New York, 2009.
[20] R. M. Darlington, T. L. McAbee, and G. Rodrigue, *A study of ALE simulations of Rayleigh-Taylor instability*, Comput. Phys. Comm., 135 (2001), pp. 58–73.
[21] B. Després and C. Mazeran, *Lagrangian gas dynamics in two dimensions and Lagrangian systems*, Arch. Ration. Mech. Anal., 178 (2005), pp. 327–372.
[22] V. A. Dobrev, T. E. Ellis, T. V. Kolev, and R. N. Rieben, *Curvilinear finite elements for Lagrangian hydrodynamics*, Internat. J. Numer. Methods Fluids, 65 (2010), pp. 1295–1310.
[23] V. A. Dobrev, T. E. Ellis, T. V. Kolev, and R. N. Rieben, *High-order curvilinear finite elements for axisymmetric Lagrangian hydrodynamics*, Comput. Fluids, (2012), doi: 10.1016/j.compfluid.2012.06.004.
[24] J. K. Dukowicz and B. J. Meltz, *Vorticity errors in multidimensional lagrangian codes*, J. Comput. Phys., 99 (1992), pp. 115–134.
[25] D. Flanagan and T. Belytschko, *A uniform strain hexahedron and quadrilateral with orthogonal hourglass control*, Internat. J. Numer. Methods Engrg., 17 (1981), pp. 679–706.
[26] S. Galera, P.-H. Maire, and J. Breil, *A two-dimensional unstructured cell-centered multi-material ALE scheme using VOF interface reconstruction*, J. Comput. Phys., 229 (2010), pp. 5755–5787.
[27] *GLVis: OpenGL Visualization Tool*, http://glvis.googlecode.com.
[28] S. Gottlieb, C. Shu, and E. Tadmor, *Strong stability preserving high order time discretization methods*, SIAM Rev., 43 (2001), pp. 89–112.
[29] F. H. Harlow and A. A. Amsden, *Fluid Dynamics: A LASL Monograph*, Tech. rep. LA-4700, Los Alamos Scientific Laboratory, 1971.
[30] C. W. Hirt, A. A. Amsden, and J. L. Cook, *An arbitrary Lagrangian-Eulerian computing method for all flow speeds*, J. Comput. Phys., 14 (1974), pp. 277–253.
[31] P. Kjellgren and J. Hyvarien, *An arbitrary Lagrangian-Eulerian finite element method*, Comput. Mech., 21 (1998), pp. 81–90.
[32] T. V. Kolev and R. N. Rieben, *A tensor artificial viscosity using a finite element approach*, J. Comput. Phys., 228 (2009), pp. 8336–8366.
[33] K. Lipnikov and M. Shashkov, *A framework for developing a mimetic tensor artificial viscosity for Lagrangian hydrocodes on arbitrary polygonal meshes*, J. Comput. Phys., 229 (2010), pp. 7911–7941.
[34] R. Loubère, J. Ovadia, and R. Abgrall, *A Lagrangian Discontinuous Galerkin-type method on unstructured meshes to solve hydrodynamics problems*, Internat. J. Numer. Methods Fluids, 44 (2004), pp. 645–663.
[35] R. Loubère, M. Shashkov, and B. Wendroff, *Volume consistency in a staggered grid Lagrangian hydrodynamics scheme*, J. Comput. Phys., 227 (2008), pp. 3731–3737.
[36] J. F. M. Feistauer and I. Straškraba, *Mathematical and Computational Methods for Compressible Flow*, Clarendon Press, Oxford, UK, 2003.
[37] P.-H. Maire, *A high-order cell-centered Lagrangian scheme for two-dimensional compressible fluid flows on unstructured meshes*, J. Comput. Phys., 228 (2009), pp. 2391–2425.
[38] P.-H. Maire, R. Abgrall, J. Breil, and J. Ovadia, *A cell-centered Lagrangian scheme for two-dimensional compressible flow problems*, SIAM J. Sci. Comput., 29 (2007), pp. 1781–1824.
[39] P.-H. Maire, R. Loubère, and P. Vachal, *Staggered Lagrangian discretization based on cell-centered Riemann solver and associated hydrodynamics scheme*, Commun. Comput. Phys., 10 (2011), pp. 940–978.

[40] L. Margolin and M. Shashkov, *Using a curvilinear grid to construct symmetry-preserving discretizaions for Lagrangian gas dynamics*, J. Comput. Phys., 149 (1999), pp. 389–417.
[41] *MFEM: Modular Finite Element Methods Library*, http://mfem.googlecode.com.
[42] W. F. Noh, *Errors for calculations of strong shocks using an artificial viscosity and an artificial heat flux*, J. Comput. Phys., 72 (1987), pp. 78–120.
[43] H. Ockendon and J. Ockendon, *Waves and Compressible Flow*, Texts in Appl. Math. 47 Springer-Verlag, Berlin, 2004.
[44] G. Scovazzi, M. Christon, T. Hughes, and J. Shadid, *Stabilized shock hydrodynamics:* I. *A Lagrangian method*, Comput. Methods Appl. Mech. Engrg, 196 (2007), pp. 923–966.
[45] G. Scovazzi, E. Love, and M. Shashkov, *Multi-scale Lagrangian shock hydrodynamics on $Q1/P0$ finite elements: Theoretical framework and two-dimensional computations*, Comput. Methods Appl. Mech. Engrg., 197 (2008), pp. 1056–1079.
[46] L. I. Sedov, *Similarity and Dimensional Methods in Mechanics*, 10th ed., Boca Raton, FL, CRC Press, 1993.
[47] R. Tipton, *CALE Lagrange Step*, Tech. rep., Lawrence Livermore National Laboratory, 1990.
[48] R. Tipton, *Hourglass Modes and a New Monotonic Hourglass Filter*, Tech. rep., Lawrence Livermore National Laboratory, 1999.
[49] J. Von Neumann and R. D. Richtmyer, *A method for the numerical calculation of hydrodynamic shocks*, J. Appl. Phys., 21 (1950), pp. 232–237.
[50] M. L. Wilkins, *Methods in Computational Physics*, vol. 3, Academic Press, New York, 1964.